

UC San Diego

UC San Diego Electronic Theses and Dissertations

Title

Chemical sensor development leading to an glucose detection method

Permalink

<https://escholarship.org/uc/item/7mr7h3t7>

Author

Caballero, Jonathan Bano

Publication Date

2008

Peer reviewed|Thesis/dissertation

UNIVERSITY OF CALIFORNIA, SAN DIEGO

Chemical Sensor Development Leading to an Alternative Glucose Detection
Method

A Dissertation submitted in partial satisfaction
of the requirements for the degree of
Doctor of Philosophy
in
Chemistry
by
Jonathan Bano Caballero

Committee in charge:

Professor Clifford P. Kubiak, Chair
Professor John Crowell
Professor Joshua Figueroa
Professor William Trogler
Professor Edward T. Yu

2008

Copyright©

Jonathan Bano Caballero, 2008

All rights reserved

The dissertation of Jonathan Caballero is approved, and it is acceptable in quality and form for publication on microfilm:

Chair

University of California, San Diego

2008

To my immediate and extended family

TABLE OF CONTENTS

Signature Page.....	iii
Dedication.....	iv
Table of Contents.....	v
List of Figures.....	viii
List of Tables.....	xi
Acknowledgements.....	xiii
Vita.....	xv
Abstract.....	xvi
Chapter 1 Chemical Sensors a Review.....	1
1.1 Introduction.....	1
1.2 References.....	12
Chapter 2 Device Fabrication.....	14
2.1 MOSFET Fabrication.....	15
2.2.1 Wafer Preparation.....	23
2.2.2 Silicon Oxide Growth.....	24
2.2.3 Wet Oxide Growth.....	25
2.2.4 Dry Oxide Growth.....	25
2.2.5 Photolithography/Patterning.....	26
2.2.6 Oxide Etch.....	27
2.2.7 Boron Predeposition and Diffusion.....	28
2.2.8 Boron Drive-In.....	29
2.2.9 Aluminum Etch.....	30

2.2.10 Thin Film Metallization	30
2.3 Fabrication of Interdigitated Electrodes	31
2.4 References	32
Chapter 3 ChemFET	33
3.1 Introduction	33
3.2 MOSFET testing	39
3.3 SAM formation	43
3.3.1 SAM formation leads to a surface potential	44
3.4 Experimental	50
3.5 Surface IR/SAM formation	52
3.6 References	56
Chapter 4 Sensor Development Using Interdigitated Electrodes	57
4.1 Introduction: Boronic acids as for diol sensing	57
4.2 Thiophene-3-Boronic Acid Binding Study	60
4.3 Preparation and X-Ray Crystallography of Thiophene Boronic Acid-Sugar Complexes	69
4.4 Conductometric Measurements of Aryl Boronic Acids	86
4.5 Experimental	88
4.5.1 Electrochemical Polymerization of thiophene 3-boronic acid	88
4.5.2 Elemental analysis of poly-thiophene boronic acid	89
4.5.3 Fluorescence Studies of poly-Thiophene 3-Boronic Acid with Alizarin Red S	89
4.5.4 Electrochemical Polymerization of Thiophene 3-Boronic Acid onto Interdigitated Electrode	89

4.5.5	Atomic Force Microscopy.....	91
4.6	Results and Discussion.....	92
4.6.1	Exposure of Thiophene 3-Boronic Acid polymer to Alizarin Red S for Fluorescence Studies.....	92
4.6.2	Interdigitated Electrode Sensing Platform.....	93
4.6.3	Electrochemical Polymerization of Thiophene 3-Boronic Acid onto Interdigitated Electrodes.....	95
4.6.4	Conditioning of the p-TBA on the Interdigitated Electrodes.....	97
4.6.5	Electrochemical Detection of Diols.....	97
4.7	Conclusion.....	101
4.8	References.....	102

LIST OF FIGURES

Figure 1-1	Lundstrom Group – Pd gated FET H ₂ sensor	4
Figure 1-2	Lieber Group – Nanowire based surface functionalized FET PSA sensor	5
Figure 1-3	Wrighton Group – Redox based conducting polymer O ₂ /H ₂ sensor	6
Figure 1-4	Lewis Group – Polymer based chemical vapor array sensor ..	7
Figure 1-5	Swager Group – Conducting polymer sensor	8
Figure 1-6	Subcutaneous glucose sensor	10
Figure 2-1	Wet oxide grown on n-type Si wafer. O ₂ bubbled through ultrapure H ₂ O at 1100 °C.	12
Figure 2-2	Source – Drain Diffusion Photomask (black) on top of photoresist covered oxide coated n-type wafer.	13
Figure 2-3	n-type silicon wafer with source and drain oxide windows opened for boron deposition.	14
Figure 2-4	Bare n-type silicon with p ⁺⁺ doped source and drain (yellow) after etching oxide layer with 10% HF solution	15
Figure 2-5	Photomask for source drain windows on top of photoresist coated device.	16
Figure 2-6	Device after coating with aluminum using E-beam.	17
Figure 2-7	Device with aluminum contacts prior to gate electrode deposition	17
Figure 2-8	Gold gated MOSFET device.	18
Figure 2-10	Wet oxide growth chart at various temperatures	21
Figure 2-11	Dry oxide growth chart at various temperatures	22
Figure 2-12	Undercutting due to over etching of oxide layer	24
Figure 2-13	Fabricated interdigitated electrodes	28

Figure 3-1	Energy band diagram for ideal MOS capacitor.....	34
Figure 3-2	Energy band diagram for ideal MOS capacitor in accumulation mode.....	35
Figure 3-3	Energy band diagram for ideal MOS capacitor in depletion mode.....	35
Figure 3-4	Energy band diagram for ideal MOS capacitor in inversion mode.....	36
Figure 3-5	Operation of a MOSFET with I-V Characteristics at small V_D ..	38
Figure 3-6	Operation of a MOSFET with I-V Characteristics at $V_D = V_{Dsat}$	38
Figure 3-7	Operation of a MOSFET with I-V Characteristics at $V_D \gg V_{Dsat}$	39
Figure 3-8	HP Parametric workstation connected to a Hewlett-Packard 4155A Semiconductor Parameter Analyzer	40
Figure 3-9	Schematic of connections to FET from grounded conducting platter, Source, Drain, and Gate contacts were made via micromanipulators	40
Figure 3-10	I_D vs V_D curves at various V_G	41
Figure 3-11	<i>p</i> -substituted phenyl isocyanides.....	47
Figure 3-12	Effect of gate biasing due to SAM formation of an e-withdrawing molecules bound to surface.....	48
Figure 3-13	Effect of gate biasing due to SAM formation of an e-donating molecules bound to surface.....	49
Figure 3-14	<i>p</i> -substituted phenyl isocyanides to be tested.....	50
Figure 3-15	IR stretch for free phenyl isocyanide (top) vs surface bound phenyl isocyanide (bottom).....	53
Figure 3-16	IR stretches of free isocyanide (2121cm^{-1}) and surface bound isocyanide (2185cm^{-1}) peaks for 1,4-phenyl diisocyanide.....	54

Figure 4-1	Formation of two component non-fluorescent binding complex of [HPTS - <i>m</i> -BBV]. Sugar binding to the <i>m</i> -BBV results in increased fluorescence due to decrease in the amount of [HPTS- <i>m</i> -BBV].	58
Figure 4-2	Stabilized benzyl diamine via sugar binding (A) vs quinone diimine (B).	59
Figure 4-3	Three component competitive binding scheme. Binding of diols to the boronic acid prevents formation of fluorescent ARS-Boronic Acid complex	61
Figure 4-4	Relative fluorescence versus the [TBA] at constant [ARS]. Graph shows characteristic fluorescence response to increasing [ARS].	62
Figure 4-5	Job's Plot binding of ARS/TBA scheme. Plot shows that there is preferential 1:1 binding between ARS:TBA.	63
Figure 4-6	Relative fluorescence versus the [ARS] shows linear response [ARS]. Since [TBA] >> [ARS] it is assumed that all ARS formed [ARS-TBA] complex thus allowing calibration for determining the concentration of ARS-TBA complex formed throughout all experiments.	64
Figure 4-7	1/[ARS-TBA] vs 1/[TBA] _{unbound} allows for determination of K _{eq} for [ARS-TBA].	65
Figure 4-8	1/P vs Q for Determination K _{eq} Glucose Slope = 217.26.	67
Figure 4-9	1/P vs Q for Determination K _{eq} Fructose Slope = 242.75.	68
Figure 4-10	X-ray crystal structure of 4,4,5,5-tetramethyl-2-thiophene-3-yl-[1,3,2] dioxaborolane, complex 1 , confirming the formation of the boronate-ester complex between pinacol and thiophene-3-boronic acid.	70
Figure 4-11	Figure 4-11 – X-ray crystal structure of 4,4,5,5-tetramethyl-2-thiophene-3-yl-[1,3,2] dioxaborolane, complex 2 , confirming the formation of the boronate-ester complex between 1,2-ethane diol and thiophene-3-boronic acid.	71
Figure 4-12	Schematic of custom made flow cell used for both electrochemical polymerization of TBA onto the interdigitated electrode platform and modified for use in the detection of diols.	90

Figure 4-13	Dual Pine Instruments Potentiostat set up for dendritic growth of pTBA across interdigitated electrodes. System employs a shared reference electrode.....	91
Figure 4-14	Image of polythiophene 3-boronic acid (top) and fluorescence image after exposure to Alizarin Red S (bottom).....	93
Figure 4-15	Schematic of Au interdigitated Electrodes with 10um separation between electrode fingers.....	94
Figure 4-16	Atomic force microscopy images of polythiophene 3-boronic acid coated and uncoated electrodes.....	95
Figure 4-17	Potential profile applied to opposing electrodes to induce dendritic growth of p-TBA.....	96
Figure 4-18	Modification of flow cell for electrochemical detection.....	97
Figure 4-19	Current response to 5mL injections of DPBS (pH 7.4) at 150mV applied potential.....	98
Figure 4-20	Current response to 5mL injections of 1.03mM glucose in DPBS followed by DPBS solutions at 150mV applied potential.....	99

LIST OF TABLES

Table 3-1	C-N Stretching frequencies for SAMs.....	52
Table 3-2	Measured I_{DS} , and V_{TH} shifts due SAM formation on gate electrode.....	55
Table 4-1	Binding constants (K_{eq}) with thiophene 3-boronic acid.....	69
Table 4-2	Crystal data and structure refinement for complex 1	72
Table 4-3	Atomic coordinates ($\times 10^4$) and equivalent isotropic displacement parameters ($\text{\AA}^2 \times 10^3$) for complex 1 . U(eq) is defined as one third of the trace of the orthogonalized U^{ij} tensor.....	73
Table 4-4	Bond lengths [\AA] and angles [$^\circ$] for complex 1	75
Table 4-5	Anisotropic displacement parameters ($\text{\AA}^2 \times 10^3$) for complex 1 . The anisotropic displacement factor exponent takes the form: $-2\pi^2 [h^2 a^{*2} U^{11} + \dots + 2 h k a^* b^* U^{12}]$	77
Table 4-6	Hydrogen coordinates ($\times 10^4$) and isotropic displacement parameters ($\text{\AA}^2 \times 10^3$) for complex 1	79
Table 4-7	Crystal data and structure refinement for complex 2	81
Table 4-8	Atomic coordinates ($\times 10^4$) and equivalent isotropic displacement parameters ($\text{\AA}^2 \times 10^3$) for complex 2 . U(eq) is defined as one third of the trace of the orthogonalized U^{ij} tensor.....	82
Table 4-9	Bond lengths [\AA] and angles [$^\circ$] for complex 2	83
Table 4-10	Anisotropic displacement parameters ($\text{\AA}^2 \times 10^3$) for complex 2 . The anisotropic displacement factor exponent takes the form: $-2\pi^2 [h^2 a^{*2} U^{11} + \dots + 2 h k a^* b^* U^{12}]$	84
Table 4-11	Hydrogen coordinates ($\times 10^4$) and isotropic displacement parameters ($\text{\AA}^2 \times 10^3$) for complex 2	85
Table 4-12	Elemental Analysis of polythiophene t-boronic acid.....	92

ACKNOWLEDGEMENTS

I was told early on in my life that there was no such thing as just being lucky, because luck is a product of *experience* meeting *opportunity*. With that being the case, I was extremely lucky over the course of my graduate career. On one level I was an *experienced* student offered the *opportunity* to attend graduate school. In the beginning of my graduate career I met Professor Kubiak. His energy, enthusiasm, and most importantly his *experience* recognized that I, a thirty year-old interested in becoming a graduate student was an *opportunity* to expand his research in the field of chemical sensors. He has influenced me to develop the skills necessary to be a scientist.

To my lab group, I could not have envision to work with a more talented and supportive group. Your willingness to share your knowledge and equally learn from mine has made this a memorable chapter in my life: Professor Casey Londergan, Dr. Catherine Salsman (J. Lynn), Dr. Hongyi Hou (The Claw), Scott Burns (Scooter), Eugenio Manso (El Chingon), Ishvaku Spencer (Kabibble), Timi Singa (Kinky), Kristina Stephenson (Sporty Spice), Dustin Seagal (PAU 1), creator of the Unbelievable Seagal of the University of California (**USUC**), Emily McLaurin (PAU 2), Jinny Kwan (PAU 3), Bridgette (PAU 4), Jackie Le (My PAU - PAU 5), Christina Hansen (PAU 6), Conner Riley (PAU 7), Dr. John Calvin Stires, III (Trifecta), Dr. BenJamIn Lear (Kracker), Jennifer Glover *aka* Starla

(Bootylicious) my little sister in the lab, John Goeltz (Goeltzy), Jonathan Smieja (Smiej), Eric Benson (Benson), Aaron Sathrum (Sathrum). I would also like to thank our assistant Melissa Hite-Miller for her patience in dealing with all the other stuff graduate students hate to deal with that don't directly deal with our academic pursuits. I consider it to be an honor to have worked with the members of the Kubiak Lab

Of this group I would especially like to thank the following: Trifecta, Kracker, and Scooter – for the countless hours of sweat and tears in the lab which will always be remembered. Starla and Goeltzy – for helping me through the final push of finishing this thesis.

And to my family, without your encouragement and support this stepping stone in my life would have never been realized. It is impossible to put into words how much I appreciate your assistance. Nothing can be truly done alone, I was just fortunate that I have my family.

I would also like to thank some of the individuals who were helpful to me with the logistics of this thesis: Ryan Anderson, Larry Grissom, and Sean Parks in the Nano III Lab at the Cal IT² facility for their experience and guidance in the cleanroom, Jeawon Park for our conversations on device fabrication, Christine Federovitch in Randy Hampton's lab in the biology department for help with the fluorescence polymer images, Katie Heroux (Angry Spice), Antonio DiPasquale,

and Professor Arnold L. Rhinegold for the crystal structures and Dr. Loren Perelman for his assistance in the fluorescence binding study.

VITA

California State University, San Diego

June 1996

Bachelors of Science in Chemistry
California State Polytechnic University Pomona

California State University, San Francisco

June 2008

Doctor of Philosophy in Chemistry
University of California, San Diego

ABSTRACT OF THE DISSERTATION

Chemical Sensor Development Leading to an Alternative Glucose Detection

Method

by

Jonathan Bano Caballero

Doctor of Philosophy in Chemistry

University of California, San Diego 2008

Professor Clifford P. Kubiak, Chair

The development of a viable sensing platform for the purpose of small molecule detection was explored on two different platforms: a Metal Oxide Semiconductor Field Effect Transistor (MOSFET) and an Interdigitated Electrode (IDE). A standard operating procedure (SOP) for the reliable fabrication of gold gated MOSFET platforms and IDE platforms was created via standard cleanroom techniques.

The n-MOSFET platform (p-channel device) drain current (I_{DS}) shifts due to the binding of a self assembled monolayer (SAM) onto the Au-gated FET. The I_{DS} directly correlates to the $(V_G - V_{TH})^2$. Binding of an electron donating p-diethylamino phenyl isocyanide SAM onto the gate results in an positive shifted I_{DS} /decreased V_{TH} , while an electron withdrawing species, 1,4-phenyl diisocyanide SAM exhibits a negative I_{DS} /increased V_{TH} . These changes in V_{TH}

shift corresponds to an electron donating species acting as a positive gate bias into the gold gate while electron acceptors acts as a negative gate bias.

Binding studies show thiophene 3-boronic acid (TBA) readily binds glucose with a binding constant of $K_{eq} = 42M^{-1}$, an order of magnitude larger than reported literature values for phenyl boronic acid. Chemical binding of 1,2-diol to poly-TBA was shown by fluorescent emission spectroscopy. Crystal structures of TBA bound to ethylene glycol and pinnacol confirm 1,2-diol binding.

An IDE platform was functionalized with thiophene 3-boronic acid (TBA) polymer via electrochemical deposition for direct detection of 1,2-diols. Conduction measurements were made upon exposure to 1,2-diol functional groups such as glucose. Buffered (pH 7.4) glucose solutions from 1 – 10 mM exhibited increases in the current across the poly-TBA, and attributed to glucose binding.

We have demonstrated by chemical, optical, and electrochemical methods that 1,2-diols such as glucose directly binds to poly-TBA and is an alternative to traditional indirect glucose detection methods.

Chapter 1

Chemical Sensors a Review

1.1 Introduction

On a daily basis we use our own built-in sensing mechanisms of sight, smell, hearing, tasting and touch. Since we use these daily, it can be taken for granted that these occur by very simplistic mechanisms. Scientist and engineers have yet to duplicate these sensing mechanisms due to the complexity of these processes. Driven by technology, there has evolved an ever present need to know everything that is around us. One such means of identifying things around us is through the use of sensors. Sensors have been implemented to accomplish tasks for precautionary (spectrometers for bomb detection at airports), and preventive (platinum wire O₂ sensors for our car exhaust systems) measures. From spectrophotometers used at airports to simple carbon monoxide detectors we have in our homes, chemical sensors play an important role in the safety of our everyday lives. As we progress, it has become obvious that a need exists for advancement of various means to sense chemicals that surround us.

Chemical sensor development requires a combination of skills found in both science and engineering. Most chemical sensors are composed of a recognition component and a transduction component. The transduction component is responsible for accepting a signal from the recognition component and converting it to a signal that can be analyzed and amplified. The processes of chemical recognition can be achieved by oxidation-reduction or by chemical binding/non-binding interactions. The recognition mechanism for most spectroscopic based sensors incorporates some sort of infrared (IR), visible light, or ultra-violet (UV) source and a detector. The detector element of the sensors generally measure absorptions of specific energy bands emitted by the source. Shifts in absorptions or emissions are directly correlated to changes due to a chemical change.

This chapter will include a brief overview of specific sensing platforms that have given me ideas and molded the research project that I developed over the course of my graduate career. It also includes representations of various chemical sensing platforms and idealized data.

Work initially pioneered by Lundstrom in 1975 opened the field of chemical sensing with newly developed semiconductor fabrication techniques. Prior to this, chemical sensing was limited only to methods where the recognition and transduction components were completely separated from each other. Due to the rapid growth of semiconductor fabrication over the years many new technologies have emerged where both recognition and transduction sensor elements have been integrated into a single component. This development has

led to shrinking sizes in chemical sensing platforms. Currently the smallest chemical sensors are in the nanoscale regime, such as the carbon nanotube based sensing platforms developed by Lieber et. al. It is from these sensing platforms that my initial work in the development of a chemically gated field effect transistor evolved.

Other important developments in the shaping of my thesis include research in conducting polymers by Shirakawa, MacDiarmid, and Heeger. Their pioneering discovery of conducting organic polymers has allowed the chemist to join in and expand on semiconductor phenomena that drives technology today. Their discoveries have allowed chemist to expand on the handful of building blocks available to semiconductor physicist. Using chemistry “tricks” the modification of the conducting polymers has been utilized to form components for variable resistors, organic light emitting diodes, and chemical sensors, just to name a few.

The initial development of chemical sensor based metal oxide semiconductor field effect transistor (MOSFET) was done by Lundstrom¹ **Figure 1-1**. The hydrogen sensitive MOSFET was developed using known CMOS device fabrication techniques.

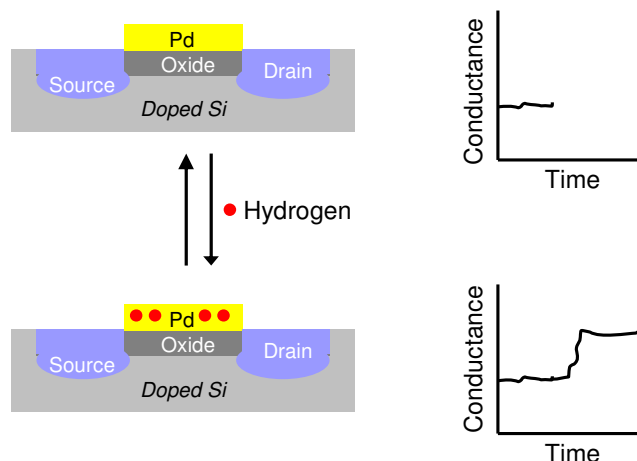
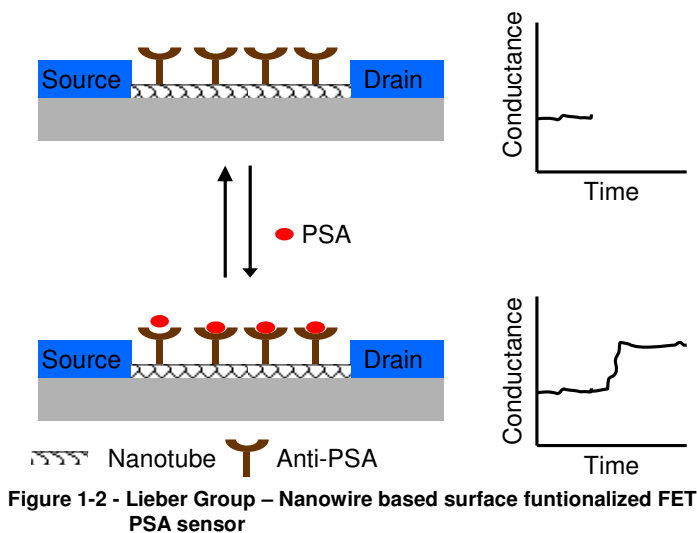


Figure 1-1 - Lundstrom Group – Pd gated FET H₂ sensor

The hydrogen sensitivity was offered by using a palladium gate, a metal known to readily adsorb hydrogen². In knowing that hydrogen can adsorb into palladium, a change in the work function of the metal gate is expected³ due to intercalation of the hydrogen within the palladium lattice. The change in the metal work function would in turn cause a shift in the threshold voltage of the MOSFET. Lundstrom had found that the hydrogen pressure can be correlated to the observed shift in threshold voltage of the FET. Although this was the first example of a chemically gated FET it is limited to small diatomics that react with catalytically active metals.

Twenty-eight years later, Lieber expanded on the FET sensing platform by demonstrating a carbon nanotube configured FET^{4, 5} **Figure 1-2.** Simple modification of



the carbon nanotube surface with an anti-prostate specific antigen (anti-PSA) allowed for the building in of the recognition element to the chemical sensor. Chemical detection was based on an analytes interaction with the surface modified nanotubes. The carbon nanotube acted as a channel to shuttle charge between source and drain electrodes. Binding interaction of a prostate specific antigen to the anti-PSA resulted in a change in the carrier mobility of the nanotube, thus affecting the nanotubes conductivity.

The discovery of conducting polymers opened the flood gates into the research of non-silicon based electronics. An important study by Wrighton et. al. investigated redox based polythiophenes across interdigitated electrodes⁶⁻⁸

Figure 1-3. Wrighton showed that the polymer could be enhanced by impregnating it with a platinum catalyst.

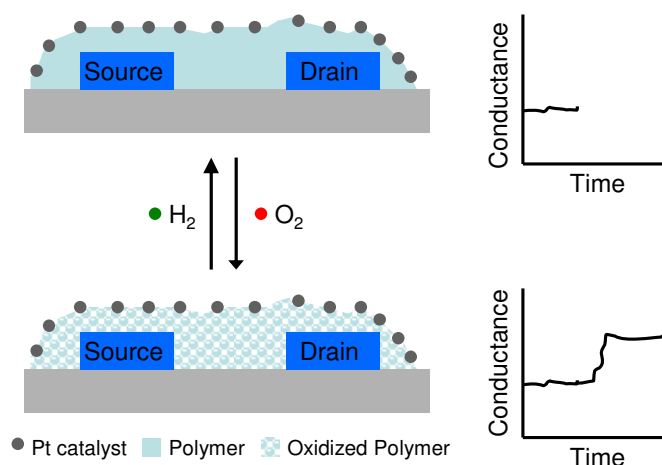


Figure 1-3 - Wrighton Group – Redox based conducting polymer O₂/H₂ sensor

The platinum impregnated polythiophene derivative exhibits catalytic sensitivity to H₂ and O₂, and acts as a redox couple with polythiophene. By controlling the redox state they were able to vary the conductivity of the polymer. In the presence of O₂, the platinum catalyzes the oxidation of the polymer. The oxidized polymer results in a change in measured conductance. Exposure of the oxidized polymer to H₂ reduces the oxidized polymer. Wrighton later showed that the polymer could be modified with any redox couple that would oxidize the polymer.

Focusing in on conducting polymers used as sensor elements, several different schemes have been employed. One such scheme is that used by Lewis^{9, 10} in his electronic nose **Figure 1-4**. Previously, measuring the change in conductivity of a specific analyte to a specific conducting polymer only allowed for the identification

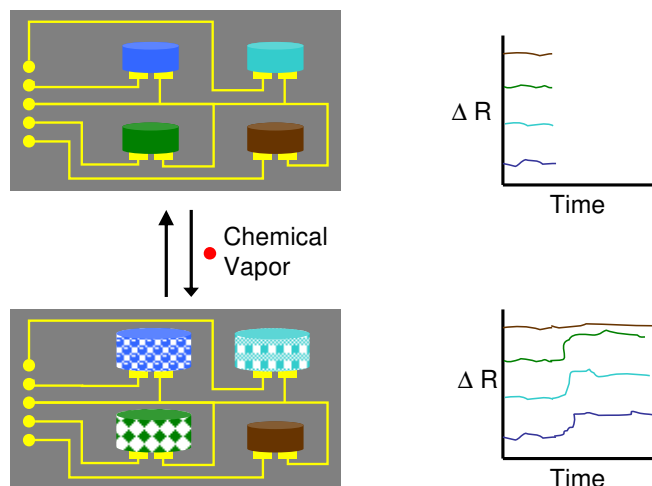


Figure 1-4 - Lewis Group – Polymer based chemical vapor array sensor

of a single component analyte. Lewis believed that the real power of identification lies not in specific binding sensors but more generalized non-specific binding sensors. Through the use of an array of non-specific binding, conducting polymer sensing elements a chemical fingerprint can be realized based on an analyte's response to each individual sensor element of the array. Lewis also showed that the array based sensor may also have inherent flexibility in identifying similar analytes based on the sensing array's response to similar families of analytes.

Another significant conducting polymer-sensing milestone was realized through the research of Swager¹¹⁻¹³. Swager's work with conducting polymers investigated the functionalization of polythiophenes with crown ether complexes. Crown ethers are known to readily form host-guest complexes with K^+ , Na^+ , and Li^+ ions. In particular, incorporation of the crown ether complex directly into the polythiophene backbone was proposed to illicit a chemoresistive response from the polythiophene. Swager has shown that a voltammetric response can be

measured from the result of host-guest chemistry of calixarenes in the presence of Li^+ and K^+ ions **Figure 1-5** and pseudorotaxenes with paraquat¹². They postulated that the presence of the guest ion produces significant degrees of charge localization within the polymer which results in reduced carrier mobility and decreased conductivity. Although they were able to measure a voltametric response in the presence of a guest, they were not able to directly correlate the response to a chemoresistive behavior of the conducting polymer. This work was the first example of a conducting pseudorotaxane as well as a demonstration of chemical recognition used to induce reversible changes in polymer conductivity.

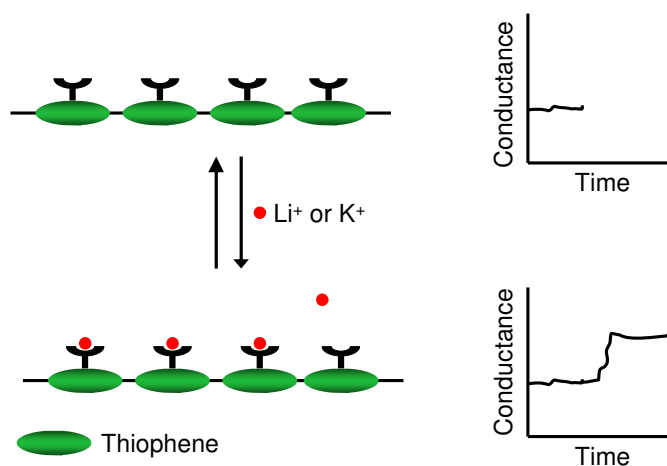


Figure 1-5 - Swager Group – Conducting Polymer Sensor

The culmination of my research revolves on the development of an alternative glucose sensor for the purpose of diabetes monitoring. Diabetes is a disease where there is a loss in the body's ability to either produce or regulate insulin resulting in elevated blood glucose levels. Elevated glucose levels can lead to serious medical complications and death. The Center for Disease Control

estimates that diabetes affects approximately 20.8 million people (~7% of the population) in the United States alone. More astounding than that is one-third of those individuals with the diabetes do not even know they have the disease.

With the help of modern medicine, individuals diagnosed with diabetes are able to live with the disease in conjunction with proper management. Monitoring of blood glucose levels requires the use of blood glucose monitors several times a day. With such a large number of the individuals having diabetes, the glucose sensor market accounts for more than 80 percent of the world market in biosensors.

One motive for developing an alternative to current blood glucose monitoring methods is that most blood glucose monitors do not directly measure the amount of blood glucose. Optically based glucose monitors indirectly determine the concentration of glucose by measuring a colorimetric change as a result of the formation of a blue benzidine derivative. Glucose oxidizes to gluconolactone in the presence of glucose oxidase with a side product of peroxide. It is the peroxide in the presence of the benzidine derivative that a blue colored benzidine polymer is developed and measured. The method's precise development protocol coupled with a high susceptibility to interfering reactions makes this method of blood glucose analysis functional but somewhat temperamental.

A more recent example of optical glucose detection is based on the binding of glucose at the end of modified optical fiber. The fiber, implanted in a patient's skin is attached to a portable analyzer that shines ultraviolet light into

the free end of the fiber **Figure 1-6**. The implanted end of the optical fiber is coated with a polyethylene-glycol polymer matrix that incorporates a fluorescent compound that is bound to dextran, a glucose like compound. Glucose has a higher affinity to the fluorescent compound than dextran and results in a change in fluorescence upon glucose binding. Quantification of glucose levels is done by measuring the change in fluorescence due to the displacement of the dextran with glucose.

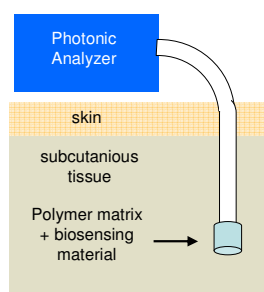


Figure 1-6 – Subcutaneous glucose detection

One alternative to an optically based glucose sensor is electrochemically based glucose sensor. In this case, a glucose oxidase coated capillary oxidizes glucose to glucolactone, while the glucose oxidase is reduced. The reduction of glucose oxidase is then quantified by re-oxidizing it with excess ferrocyanide. Although fairly accurate, this method still incorporates an indirect measurement of glucose.

My research into the development of an alternative glucose detector incorporated an electrochemical based sensing element that integrates both the chemical recognition and transduction element into a simplified unit. More

importantly, it utilized a recognition element that directly detects glucose. In doing so I was able to incorporate the fabrication techniques from my initial work on the development of a chemically gated field effect transistor (ChemFET). Though my initial ideas for a ChemFET sensor platform did not work out as planned, I was still able to use the semiconductor fabrication techniques to help me develop my glucose detector.

REFERENCES

1. Lundstrom, *Applied Physics Letters* **1975**, 26, (2), 15.
2. Lewis, F. A., *The Palladium Hydrogen System*. Academic Press: New York, 1967.
3. Horiniti, J.; Toga, T., *Solid State Surface Science*. Marcel Dekker: New York, 1969.
4. Patolsky, F.; Timko, B.; Zheng, G.; Lieber, C., Nanowire-based nanoelectronic devices in the life sciences *MRS Bulletin* **2007**, 27, 143-149.
5. Patolsky, F.; Zheng, G.; Lieber, C. M., Fabrication of silicon nanowire devices for ultrasensitive, label-free, real-time detection of biological and chemical species. *Nature Protocols* **2006**, 1, 1711-1724.
6. Thackeray, J. W.; White, H. S.; Wrighton, M. S. *Poly-3-methylthiophene coated electrodes. Optical and electrical properties as a function of redox potential and amplification of electrical and chemical signals using poly-3-methylthiophene-based microelectrochemical transistors*; Dep. Chem., Massachusetts Inst. Technol., Cambridge, MA, USA.: 1985; p 36 pp.
7. Thackeray, J. W.; Wrighton, M. S., Chemically responsive microelectrochemical devices based on platinized poly(3-methylthiophene): variation in conductivity with variation in hydrogen, oxygen, or pH in aqueous solution. *J. Phys. Chem. FIELD Full Journal Title:Journal of Physical Chemistry* **1986**, 90, (25), 6674-9.
8. Wrighton, M. S.; White, H. S., Jr.; Thackeray, J. W. Molecule-based microelectronic devices. 85-114866 185941, 19851123., 1986.
9. Lonergan, M. C.; Severin, E. J.; Doleman, B. J.; Beaver, S. A.; Grubbs, R. H.; Lewis, N. S., Array-based vapor sensing using chemically sensitive, carbon black-polymer resistors. *Chem. Mater. FIELD Full Journal Title:Chemistry of Materials* **1996**, 8, (9), 2298-2312.
10. Severin, E. J.; Doleman, B. J.; Lewis, N. S., An investigation of the concentration dependence and response to analyte mixtures of carbon black/insulating organic polymer composite vapor detectors. *Anal. Chem. FIELD Full Journal Title:Analytical Chemistry* **2000**, 72, (4), 658-668.
11. Marsella, M. J.; Carroll, P. J.; Swager, T. M., Conducting Pseudopolyrotaxanes: A Chemoresistive Response via Molecular Recognition. *J.*

Am. Chem. Soc. FIELD Full Journal Title:Journal of the American Chemical Society **1994**, 116, (20), 9347-8.

12. Marsella, M. J.; Carroll, P. J.; Swager, T. M., Design of chemoresistive sensory materials: polythiophene-based pseudopolyrotaxanes. *J. Am. Chem. Soc. FIELD Full Journal Title:Journal of the American Chemical Society* **1995**, 117, (39), 9832-41.

13. Marsella, M. J.; Newland, R. J.; Carroll, P. J.; Swager, T. M., Ionoresistivity as a highly sensitive sensory probe: investigations of polythiophenes functionalized with calix[4]arene-based ion receptors. *J. Am. Chem. Soc. FIELD Full Journal Title:Journal of the American Chemical Society* **1995**, 117, (39), 9842-8.

Chapter 2

Device Fabrication

An advisor has reminded me several times that the difference between chemistry and engineering is that at the end of the day, chemists make stuff. In the process of my work, I have learned that engineers make stuff too. As a chemist, we use our knowledge of chemical properties to develop a system that can solve a problem such as the development of a chemical sensor. And it is through our knowledge of chemical properties that we know that modifying benzene by: a) adding a halogen group will leave the benzene ring electron deficient or b) adding an amine group will leave a benzene ring electron rich.

Our assumptions of engineers are that they envision something, make lots and lots of calculations but then someone else makes whatever they calculated. My work has allowed me to get just a taste of the work that engineers do and has given me an appreciation behind all the calculating. In the process of making devices for the purpose of chemical sensing I have learned that all of the calculating minimizes the amount of time spent trying to figure out why a device does not work.

As I mentioned above, my work has allowed me to get a taste of the work that engineers do. I doing so I have learned the processes for the development of test platforms using semiconductor fabrication techniques. In the following chapter I will outline the process of device fabrication of a metal oxide semiconductor field effect transistor (MOSFET) and interdigitated electrodes. I will also cover the methods used to test the devices.

2.1 MOSFET Fabrication

The first step of any device fabrication is cleaning of the platform to ensure that minimal contaminants are present (see Wafer Preparation). This assures a consistent starting point for device fabrication, ultimately resulting in a high yield process with reproducible device characteristics.

The next step is to create the source and drain regions of the field effect transistor (FET). Since we are using a n-type wafer our device is thus a p-channel FET. In the n-type wafer where a p-channel is formed, the main charge carriers are holes. The source and drain regions on the FET are thus composed of highly doped boron regions (p^{++}) that act as ohmic contacts between an aluminum contact and the semiconductor. The p^{++} region is formed by highly doping the semiconductor with boron¹. In order to control where the highly doped regions are formed a very thick oxide layer of SiO_2 needs to be grown onto the silicon surface. The thick oxide layer is used as a diffusion mask to

prevent the spreading of dopant onto unwanted regions of the device (see Wet Oxide Growth).

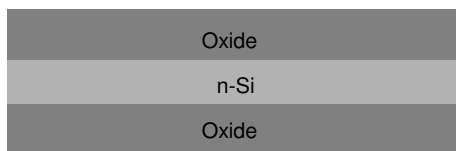


Figure 2-1 - Wet oxide grown on n-type Si wafer. O₂ bubbled through ultrapure H₂O at 1100 °C.

After the oxide is grown **Figure 2-1** the wafer is cleaned on a spin coater rotating at 6000 rpms. Successive dousing with acetone, ethanol, methanol, and then ultra pure water (UPW) while mechanically agitating with a swab allows for removal of any organics followed by an UPW rinse. The wafer is then baked at 110°C to remove any residual water that could later lead to premature liftoff of the photoresist.

Photoresist (Shipley Microposit S1818) is spin coated onto the wafers at 6000 rpm for 20 seconds. The resulting photoresist coats the entire wafer surface and is approximately 1µm thick. A photomask made of chromium on soda lime glass is placed onto of the wafer **Figure 2-2** and the wafer is exposed using contact photolithography on an HTG Mask Aligner. The substrate is baked for 30 seconds at 110°C to increase adhesion of the unexposed

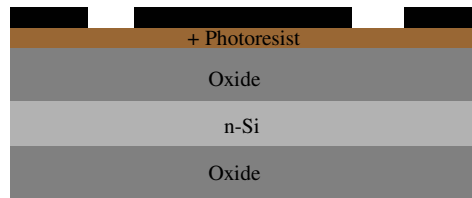


Figure 2-2 - Source – Drain Diffusion
Photomask (black) on top of photoresist
covered oxide coated n-type wafer.

photoresist to the substrate. The exposed photoresist is then chemically removed using a 50:50 solution of UPW:ShIPLEY Microdeposit MP Dev for 30 seconds with light agitation. The wafer is then immediately immersed in streaming UPW for 1 minute and then the substrate is blown dry with ultra pure nitrogen.

The wafer is then baked at 110°C to remove any residual water that can cause lift-off of the photoresist coating resulting in inaccurate duplication of the desired pattern. The photoresist patterned wafer is then immersed in a buffered oxide etch. The buffered oxide etch controls the rate of etching and minimizes undercutting of the desired pattern. One trick to minimize over etching is to look at the hydrophobicity of bare silicon versus silicon oxide. On a SiO_x coated surface, water will form hydrogen bonds to the oxygen atoms of the SiO_2 thus wetting the surface. Water does not hydrogen bond to bare Si, a hydrophobic surface, and will bead up. Since the reverse side of the wafer is coated with exactly the same amount of oxide, on the front, over-etching can be avoided by stopping etching when the reverse side of the wafer has become hydrophobic.

The wafer is then immediately rinsed in UPW followed by drying with ultra pure nitrogen.

Now that the location for the source and drain regions for the device are the only exposed areas of bare silicon **Figure 2-3**, steps for the pre-deposition of boron and subsequent drive-in can be done (See Boron Pre-Deposition and

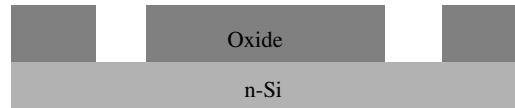


Figure 2-3 – n-type silicon wafer with source and drain oxide windows opened for boron deposition.

Boron Drive-In). Boron pre-deposition implants boron atoms onto an adjacent surface via lateral diffusion from a boron source. The subsequent boron drive-in diffuses the implanted boron into the semiconductor and results in boron atoms taking positions within the semiconductor lattice, leading to local p-doping of the semiconductor.

The process of boron drive-in incorporates the flowing of O_2 bubbled through UPW into the furnace resulting in the formation of a thick oxide layer. The thick oxide layer impedes diffusion of the implanted boron off of the surface during the drive-in step and forces boron diffusion into the wafer. After the boron drive-in step, the wafer is cleaned in 10% Hydrofluoric Acid (HF) in UPW followed by a one minute rinse in flowing UPW and then blown dry in pure $N_2(g)$.

The result is a device with p++ doped source and drain regions **Figure 2-4**. The wafer is immediately put into a dry furnace with a flow of dry O_2 (500cc/min)



Figure 2-4 - bare n-type silicon with p++ doped source and drain (yellow) after etching oxide layer with 10% HF solution

for one hour (see Dry Oxide Growth). The result is a SiO_2 oxide layer that makes up the gate oxide with a thickness of approximately 100nm.

The wafer is then immediately coated with photoresist (Shipley Microposit S1818 6000 rpms for 20 seconds). The Source-Drain Window Photomask is placed onto the wafer **Figure 2-5** and the wafer is exposed using an HTG Mask Aligner. The substrate is baked for 30 seconds at 110°C to increase adhesion of the photoresist to the substrate. The exposed photoresist is then chemically

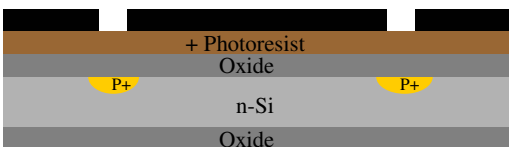


Figure 2-5 - Photomask for source drain windows on top of photoresist coated device.

removed using a 50:50 solution of UPW:Shipley Microdeposit MP Dev for 30 seconds with light agitation. The wafer is then immediately immersed in streaming UPW for 1 minute and then the substrate is blown dry with ultra pure nitrogen.

The resulting wafer is now a photoresist covered device with openings in the photomask to allow etching of the dry oxide for the purpose of making physical connections to the p++ source and drain regions.

The wafer is then baked at 110°C to remove any remaining water and increase adhesion of the photoresist to the surface. The photoresist patterned wafer is immersed in a buffered oxide etch until the backside of the wafer is hydrophobic. The wafer is then immediately rinsed in UPW followed by drying with ultra pure nitrogen.

Wafers are then placed in a solution of warm acetone and agitated to facilitate the removal of the remaining photoresist. They are rinsed in UPW followed by subsequent drying with ultra pure nitrogen.

Wafers are immediately loaded into a thin film metallization system for deposition of aluminum (see Thin Film Metallization) source and drain contacts. A thin film of aluminum (approximately a 250-400nm) is deposited onto the surface **Figure 2-6** followed by spin coating of the photoresist. The Source-Drain

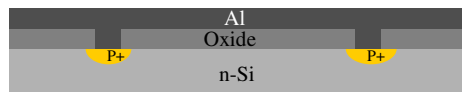


Figure 2-6 – Device after coating with aluminum using E-beam.

Contact Photomask is placed onto the wafer and the wafer is exposed using an HTG Mask Aligner. The substrate is baked for 30 seconds at 110°C to increase adhesion of the photoresist to the substrate. The photoresist is then chemically removed using a 50:50 solution of UPW:Shipley Microdeposit MP Dev for 30 seconds with light agitation. The wafer is then immediately immersed in streaming UPW for 1 minute and then the substrate is blown dry with ultra pure

nitrogen. The device is hard baked at 110°C for 15 minutes to further improve adhesion of the photoresist.

Wafers are then placed in an aluminum etch solution (see Aluminum Etch) until the dark color of the gate oxide shows thru, leaving only islands of aluminum, the desired source-drain contact pads. Removal of the photoresist is facilitated by agitation in warm acetone followed by sonication for thirty seconds. Wafers are rinsed with UPW for one minute and dried using UPN. The resulting device has p++ doped regions that are covered with aluminum contacts **Figure 2-7**.

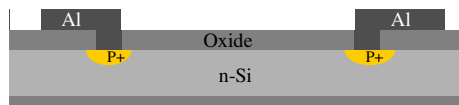


Figure 2-7 – Device with aluminum contacts prior to gate electrode deposition

The wafer is then immediately coated with photoresist. The Gate Photomask is placed onto the wafer and the wafer is exposed using an HTG Mask Aligner. The substrate is soft baked for 30 seconds at 110°C to increase adhesion of the photoresist to the substrate. The exposed photoresist is then chemically removed using a 50:50 solution of UPW:ShIPLEY Microdeposit MP Dev for 30 seconds with light agitation. The wafer is then immediately immersed in streaming UPW for 1 minute and then the substrate is blown dry with ultra pure nitrogen.

The resulting wafer is now a photoresist covered device with openings in the photomask to allow for the deposition of the gate electrode. Wafers are

immediately loaded into a thin film metallization system for deposition of the gold gate electrode (see E-Beam Thin Film Deposition). Approximately 15nm of titanium (as an adhesion layer) immediately followed by 100-150nm thin film of gold is deposited onto the surface. Wafers are then placed in a solution of warm acetone to facilitate the removal of the photoresist, including the gold coated photoresist. They are sonicated for approximately 30 seconds to assist in the removal of residual photoresist followed by rinsing in UPW for 1 minute and then N₂ dried. The resulting device is the gold gated MOSFET **Figure 2-8**.

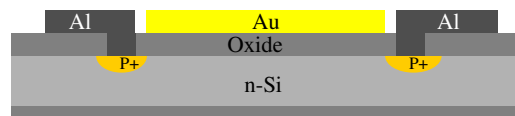


Figure 2-8 – Gold gated MOSFET device.

The device side of the wafer is then coated with photoresist and baked for 5 minutes at 110°C. The wafers are then placed in buffered oxide etch (BOE) until the backside of the wafers are hydrophobic to remove the oxide growth. The wafer is then immediately immersed in streaming UPW for 1 minute and then the substrate is blown dry with UPN. Wafers are immediately loaded into a thin film metallization system for deposition of aluminum (see Thin Film Metallization) on the backside of the wafers. This aluminum acts as a backside contact for the device.

The wafer is then placed in a furnace to anneal the device as well as alloy the aluminum contacts to the p⁺⁺ regions. The alloying results in ohmic contacts between the aluminum and the p⁺⁺ doped regions on the device. At this step, a

gold-gated MOSFET has been fabricated. The main difference from a standard MOSFET is the gold gate allows us to do various surface chemistries such as SAM formation with thiols and isocyanides.

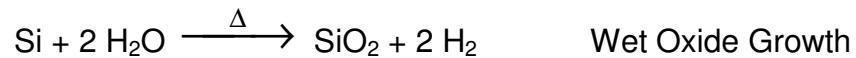
2.2.1 Wafer Preparation

The process to remove contaminants on the surface of silicon wafers has been developed in order to obtain high performance and reliable semiconductor devices. Silicon wafer surface contaminants are remnants from previous processing steps and must be removed to not only assure a clean platform for device fabrication, but also to prevent contamination of processing equipment. A method developed by Werner Kern while working at RCA (Radio Corporation of America) has been adopted as the basic procedure in for wafer cleaning^{2,3}.

Wafers are initially etched for 30 seconds in a 5% hydrofluoric acid (HF) solution in UPW in order to remove any native oxide layer that has grown on to the surface⁴. HF etching does not attack the silicon, but it selectively etches SiO₂. Wafers are then immersed in running UPW for 1 minute to quench the reaction as well as to remove any contaminants. Wafers are then immersed for 10 minutes in a 70+/-5°C solution composed of 5 parts UPW, 1 part 27% ammonium hydroxide (NH₄OH) and 1 part 30% hydrogen peroxide (H₂O₂). This solution removes residual organic contaminants from the wafer surface while creating a thin silicon dioxide (SiO₂) layer to further protect the wafer surface from other contaminants. This step is followed by rinsing of the wafers with UPW. Wafers are then immersed in a 10% HF solution to remove the formed

oxides. They are then immersed for 10 minutes in $70\pm 5^\circ\text{C}$ solution composed of 1 part hydrochloric (HCl (conc.)), 2 parts H_2O_2 , and 5 parts UPW to remove any metallic contaminants. Wafers are rinsed under UPW for 1 minute and then blown dry with UPN. Wafers are visually inspected to assure that no residual deposits are left on the surface.

2.2.2 Silicon Oxide Growth



SiO_2 is used for two purposes in semiconductor fabrication, either as sacrificial masks or as insulating layers. As a sacrificial mask, it is generally preferred to grow a wet oxide due to the higher rate of oxide growth as compared to rate of dry oxide growth. Wet oxide growth generally occurs at a rate that is ten times that of the dry oxide growth. Dry oxide growth is preferred when the required thickness of the oxide layer is specific and the quality of oxide is important.

Preparation of the oxidation furnace is necessary in order to get even, reproducible oxide layers. Growth rate of a wet oxide is primarily done when a thick oxide layer is necessary with a minimal amount of time.

2.2.3 Wet Oxide Growth

Dry O_2 is bubbled (500cc/min) through heated $17M\Omega$ H_2O ($95^\circ C$) and pushed into a furnace that is maintained at $1000^\circ C$. Wafers are loaded onto a quartz boat and are slowly introduced to the furnace. Introduction of the wafers to the furnace must occur at a slow rate so as to not produce thermal shock to the wafers that result in cracking and/or shattering of the wafers. After the desired oxide thickness has been grown **Figure 2-10**, removal of the wafers from the furnace should also occur at a rate slow enough as to not thermally shock the wafers.

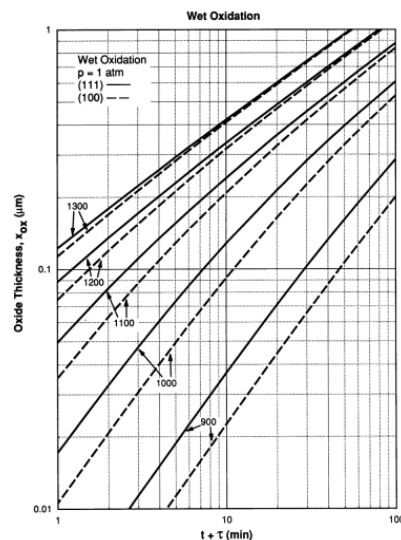


Figure 2-10 – Wet Oxide Growth Chart at various temperatures

2.2.4 Dry Oxide Growth

Dry oxide growth only differs from wet oxide growth in that dry O_2 is pushed into a furnace that is maintained at $1000^\circ C$ but is not bubbled through water. The dry oxide is the most critical component of the MOSFET because it makes up the gate oxide. It is imperative that sample conditions are kept

consistent. Dry oxide growth must be done in a furnace which is not used for any other purpose than dry oxide growth. Any residual water from a wet oxide growth in the same furnace can lead to inconsistencies in the gate oxide.

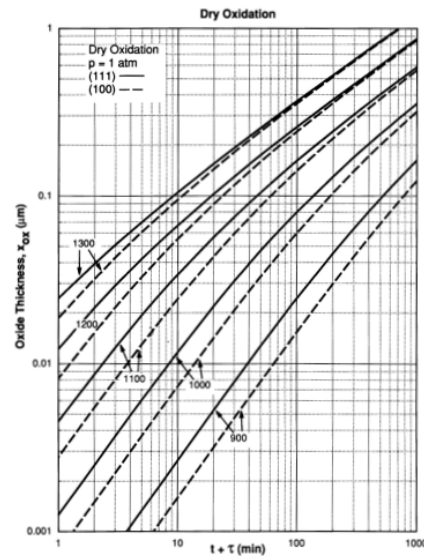


Figure 2-11 – Dry Oxide Growth Chart at various temperatures

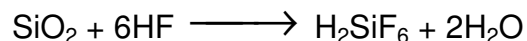
Depending on the desired thickness of the oxide layer, wait times can be estimated using standard oxide growth charts **Figure 2-11**. It is imperative to check the oxide thickness, particularly when laying down the gate oxide. Confirmation of the oxide thickness is done via a Filmetrics F20 thin film measurement system, which measures the spectral reflectance of the oxide layer on the Si wafer.

2.2.5 Photolithography/Patterning

The HTG Mask aligner is used for photolithography and is an essential component in microscale fabrication. The technology involves transferring a

pattern from a master to a substrate. The master (mask) can be aligned to existing patterns on the platform using micromanipulators. The pattern transfer is done by covering the substrate with photoresist and exposing to UV light through the mask. Exposure to the UV light results in degradation of the light sensitive polymer (in the case of positive photoresist), that can be developed/chemically removed later. This results in a photoresist pattern matching that of the master. The substrate with photoresist can then be baked to make the unexposed photoresist impervious to acids and other chemicals. The pattern is permanently transferred to the substrate by other processes such thin film metallization using e-beam lithography or modification of existing layers on the device using chemical etching techniques. Later removal of the photoresist is done by agitating the platform in solvents such as acetone.

2.2.6 Oxide Etch



Removal of the oxide layer is done using a dilute hydrofluoric acid solution and does not affect the Si platform. The oxide removal can be performed in either buffered or unbuffered solutions of hydrofluoric acid. Unbuffered oxide etch is used when the process requires the complete removal of all SiO_2 . Unbuffered oxide etch is done using a 5 – 10% HF solution in UPW. Buffered oxide etch is a ammonium fluoride buffered HF solution in UPW. Buffered oxide etch (BOE) is used when the process requires the controlled removal of oxide.

The rate of buffered etching is generally measured using a sacrificial oxide coated wafer with known oxide thickness. Measuring the change in thickness of an oxide layer on a sacrificial oxide coated wafer before and after exposure to a buffered solution for a given amount of time allows for the calculation of the oxide etching rate. Knowing the oxide etch rate is necessary to prevent over etching of the oxide layer. Overetching leads to undercutting of the oxide below the photoresist mask and inaccurate duplication of the photomask as depicted in **Figure 2-12**.

Figure 2-12.



Figure 2-12 – Undercutting due to over etching of oxide layer

2.2.7 Boron Predeposition and Diffusion

Deposition and subsequent diffusion of boron onto a silicon surface allows localized doping of a semiconductor. Initially boron diffuses from the boron source in the form of B_2O_3 to the silicon surface forming a borosilicate glass.



The high, local concentration of borosilicate glass results in a concentration gradient on the silicon. The concentration gradient will cause diffusion of the borosilicate glass into the silicon wafer under high temperature conditions. The process alters the semiconductor lattice by introducing boron atoms into the semiconductor lattice. This in turn changes the resistivity of the semiconductor.

High doping of the semiconductor eventually leads to a more metallic-like semiconductor, which when mated to a metallic contact and alloyed, facilitates the transfer of charge and forms an ohmic bridge to the contact.

Predeposition of boron begins with the conditioning of clean boron nitride wafers (Carborundum Company) at 975°C under a stream of ultra pure O₂ (500cc/min) for 45 minutes. The process grows a coating of boron oxide (B₂O₃) on the surface of the boron nitride wafers. The wafers are then stabilized by turning off the O₂ and flowing dry N₂ (500cc/min) for 60 minutes at 975°C. Deposition of boron onto the desired wafers is done by a lateral diffusion process. The side to be coated with boron is placed facing the conditioned B₂O₃ coated BN wafers in the 975°C furnace for 1 hour under a stream of N₂ (2000cc/min). B₂O₃ diffuses to the surface of the wafer and coats both bare silicon and silicon oxide regions on the surface. When an adequate amount of boron is deposited onto the surface, the BN wafers are removed. The silicon wafers are then oxide etched in a 10% HF solution in UPW until the wafer is hydrophobic. This step etches off the SiO₂ and any boron that was deposited into the oxide layer. Any remaining boron lies on the designated source and drain region of the device and is ready for the drive-in process.

2.2.8 Boron Drive-In

Drive-in of the boron onto the semiconductor surface is done under a wet oxide conditions to induce growth of a thick oxide layer. The thick oxide layer minimizes the outward diffusion of any deposited boron, thus forcing

predeposited boron into the wafer. The initial oxide layer is formed by bubbling O_2 (500cc/min) thru UPW (95°C) into a 975°C furnace for 4 hours. Wafers are then removed and HF etched to remove any oxides.

2.2.9 Aluminum Etch

Aluminum etchant is composed of 80 mL concentrated phosphoric acid (H_3PO_4), 20 mL UPW, and 5 mL of nitric acid (HNO_3)⁵. The solution will etch aluminum at approximately 100nm/min at room temperature. It is important to note that the sample must be agitated. Samples are rinsed with UPW for one minute and then blow dry with ultra pure nitrogen.

2.2.10 Thin Film Metallization

Thin film metallization is done with a Temescal BJD 1800 Evaporator. Wafers are placed on an inverted sample holder that faces the desired metal source, the Temescal BJD 1800 allows for loading up to 4 different metal sources that can be rotated externally to allow for layering of different metals. Through a series of pump downs, vacuum is established within the chamber to approximately 1.0×10^{-6} Torr. Using a focused electron beam, metal particles are ejected from the sample holder out towards the sample. Thickness of the thin metal film is measured using a quartz crystal microbalance adjusted for the particular metal being evaporated. Some metals such as gold require an adhesion layer such as titanium to assist in adhesion. Aluminum does not require an adhesion layer.

2.3 Fabrication of Interdigitated Electrodes

Interdigitated electrodes are fabricated by spin coating a clean (see Wafer Preparation) oxide coated wafer (~100 nm oxide layer) with photoresist at 6000 rpms for 20 seconds. The Interdigitated Electrode Photomask made of chromium on soda lime glass is placed onto of the wafer and the wafer is exposed using contact photolithography on an HTG Mask Aligner. The substrate is baked for 30 seconds at 110°C to increase photoresist adhesion. The exposed photoresist is then chemically removed using a 50:50 solution of UPW:Shipley Microdeposit MP Dev for 30 seconds with light agitation. The wafer is then immediately immersed in streaming UPW for 1 minute and then the substrate is blown dry with ultra pure nitrogen.

The resulting wafer is now a photoresist covered device with openings in the photomask to allow for the deposition of the interdigitated electrodes. Wafers are immediately loaded into a thin film metallization system for deposition of the gold gate electrode (see E-Beam Thin Film Deposition). Approximately 15nm of titanium (as an adhesion layer) immediately followed by 100-150nm thin film of gold is deposited onto the surface. Wafers are then placed in a solution of warm acetone for one minute to facilitate the removal of the photoresist, including the gold coated photoresist. They are sonicated for approximately 30 seconds to assist in the removal of residual photoresist followed by rinsing in UPW for one minute and then N₂ dried. The resulting device is the gold interdigitated electrodes **Figure 2-13**.

REFERENCES

1. Card, H. C., One-Dimensional Analysis of Heat Treated Aluminum-Silicon Junctions *Inst. Phys. Conf. Ser., (Met.-Semicond. Contacts, Proc. Conf.)* **1974**, 22, 129-137.
2. Kern, W.; Vossen, J., *Thin film Processes*. Academic Press: New York, 1978.
3. Kern, W., *Handbook of Semiconductor Cleaning Technology*. Noyes Publishing: Park Ridge, NJ, 1993.
4. Spierings, G. A. C. M., Wet chemical etching of silicate glasses in hydrofluoric acid based solutions. *Journal of Materials Science* **1993**, 28, (23), 6261-73.
5. Minford, J. D., *Handbook of Aluminum Bonding Technology and Data*. CRC: 1993.

Chapter 3

ChemFET

3.1 Introduction MOSFET

The development of the Metal Oxide Semiconductor Field Effect Transistor (MOSFET) in 1963¹ has been one of the key semiconductor device architectures for the advancement of integrated circuits. The MOSFET's ability to be readily scaled down in size² as well as its low power consumption has also made it one of the most researched device architectures. In order to utilize the MOSFET for sensor development it is essential to understand the basic components that make a MOSFET.

The MOSFET is essentially a MOS capacitor with the semiconductor sandwiched between a source and drain electrode, forming two p-n junctions. The ideal MOS capacitor depends on two variables, the doping of the semiconductor and the capacitance of the oxide layer. Looking at the energy band diagram for an ideal MOS capacitor where a metal is separated from doped silicon by an insulating oxide of thickness d **Figure 3-1** assuming p-type semiconductor. At zero applied bias the Fermi levels E_F of the metal and the

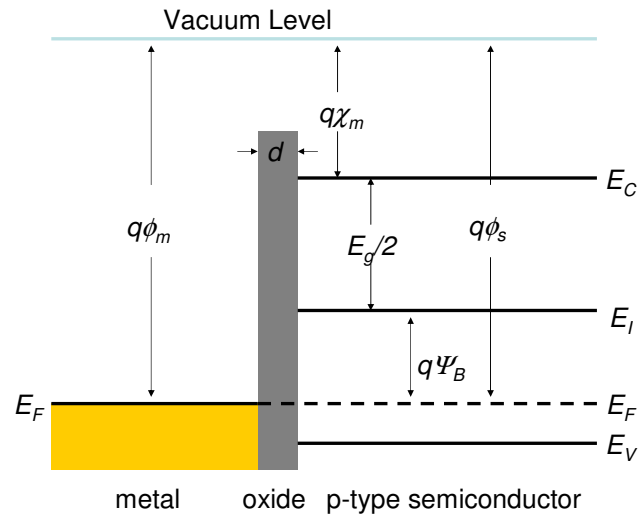


Figure 3-1 - Energy band diagram for ideal MOS capacitor

semiconductor are aligned and their difference is zero, $q\phi_{ms} = 0$ Equation 3-1 where ϕ_m = work function of the metal and ϕ_s is the work function of the semiconductor.

$$q\phi_{ms} = q\phi_m - q\phi_s \quad \text{Equation 3-1}$$

When the metal is biased, there are three cases that may exist within the semiconductor: accumulation, depletion, and inversion. Accumulation mode is the result of applying a negative voltage to the metal $V_G < 0$. Under these conditions, the negative charge on the metal induces a field near the semiconductor-insulator interface that draws out holes from the semiconductor to the semiconductor-insulator interface. Under accumulation mode the bands are bent upward **Figure 3-2**. In depletion mode a small positive voltage is applied to

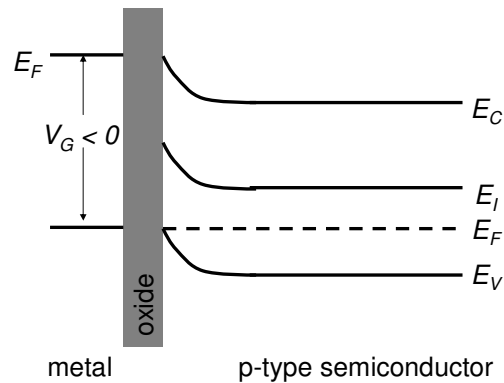


Figure 3-2 - Energy band diagram for ideal MOS capacitor in accumulation mode

the metal $V_G > 0$ such that the intrinsic level E_i bends down to the original E_F of the semiconductor **Figure 3-3** and the majority carrier are depleted from the

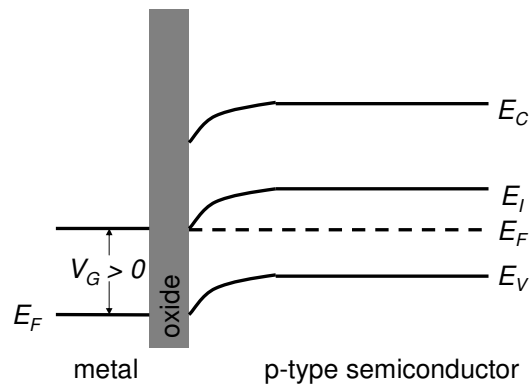


Figure 3-3 - Energy band diagram for ideal MOS capacitor in depletion mode

semiconductor-insulator interface. In the inversion mode, a larger bias positive bias is applied $V_G \gg 0$ such that the intrinsic level E_i bends down past the original E_F of the semiconductor **Figure 3-4**. The V_G at the initial onset of inversion is

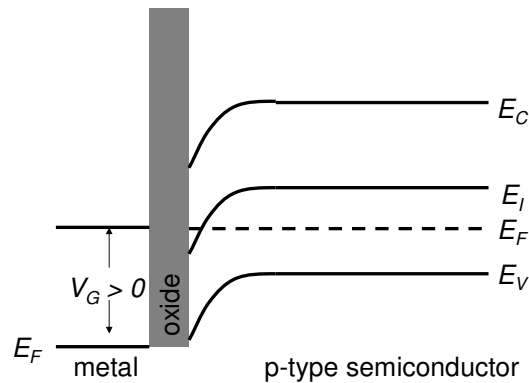


Figure 3-4 - Energy band diagram for ideal MOS capacitor in inversion mode

referred to as the threshold voltage V_{TH} and will be explained later. In the inversion mode the large positive bias begins to induce excess negative charge out of the bulk of the semiconductor and into the semiconductor-insulator interface, thus forming an n-channel.

As stated previously, the MOSFET is essentially a MOS capacitor with the semiconductor sandwiched between a source and drain electrode, forming two p-n junctions. The source and drain regions are generally highly doped n^{++} regions for n-channel devices and p^{++} doped for p-channel devices. In this example the source and drain are composed of n^{++} regions with p-type silicon between forming a n-p-n junction. Due to the length of the channel region between the source and drain electrodes of the MOSFET's the n-p-n junction can be broken down into two separate p-n junctions. Onset of inversion mode converts the channel region from p-type to n-type, thus forming an n-channel between the two n^{++} regions, source and drain, allowing charge to flow.

The initial onset of inversion mode where just a small amount of charge flows between the source and drain is comparable to the turning on of a faucet in which only a trickle of water flows. As a larger potential is applied to V_G , the size of the channel increases, allowing more charge to flow between source and drain. As in the case of a faucet, there is a maximum flow allowed even though the faucet is opened all the way, due to the size of the pipe delivering the water. The size of the pipe compares to the size of the channel formed by applying a larger bias to the V_G . The channel formed to shuttle charge between source and drain maxes out at the point of strong inversion because the amount of band bending becomes so great that any further bending only leads to negligible gains in the channel width.

The shuttling of charge between the source and drain is not only governed by the channel width induced by the applied V_G . The bias on the drain V_D results in the formation of depletion region around the drain-semiconductor/source-semiconductor interface that has adverse effect on the channel. Upon onset of inversion, increases in the V_D will result in a linear increases in the drain current I_D **Figure 3-5** and is referred to as the linear region of the I_D vs V_D plot. As V_D

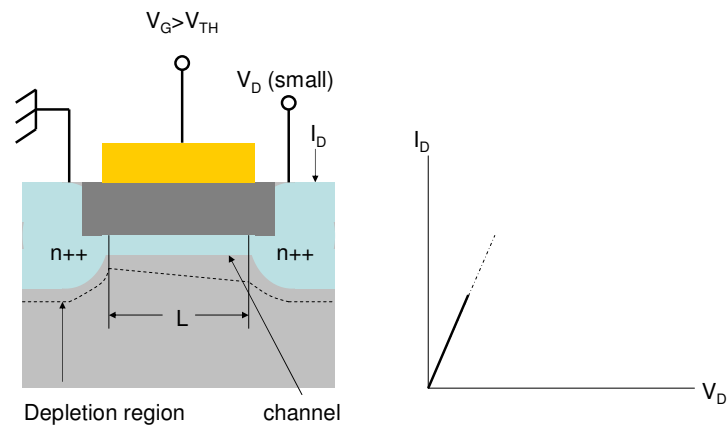


Figure 3-5 – Operation of a MOSFET with I-V Characteristics at small V_D

increases a larger depletion region around the drain electrode develops and as a result leads to pinching off of the channel region near the drain electrode **Figure 3-6**. The pinching off of charge is due to the increased size of the depletion region surrounding the drain electrode thus limiting the amount of charge carriers

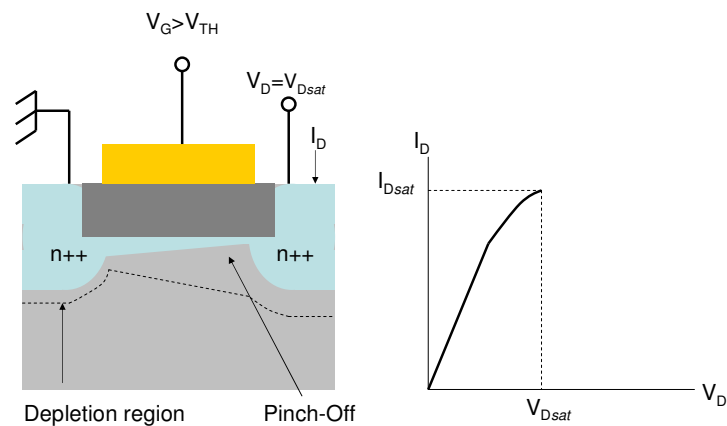


Figure 3-6 – Operation of a MOSFET with I-V Characteristics at $V_D = V_{Dsat}$

in the vicinity. The decreased rate of current flow is expected as a result of the pinching off until the applied V_D reaches the drain saturation voltage V_{Dsat} .

Further increases in the $V_D \gg V_{Dsat}$ will no longer exhibit increases in the I_D

Figure 3-7.

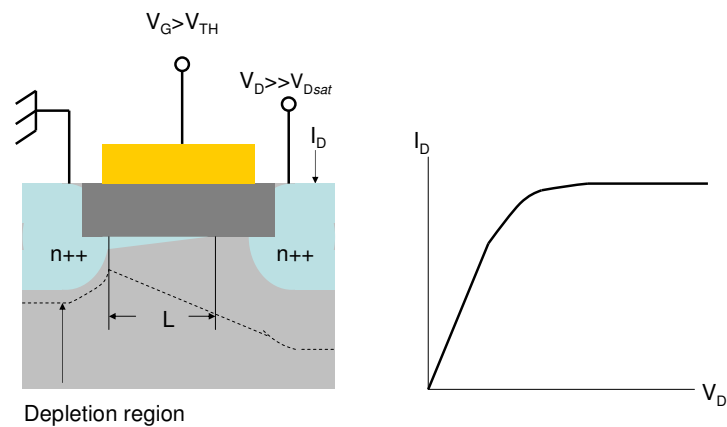


Figure 3-7 – Operation of a MOSFET with I-V Characteristics at $V_D \gg V_{Dsat}$

Now that an understanding of the basic operation of MOSFET is clear the focus of my research on the development of a chemical sensing MOSFET will lie primarily in the linear region. The linear region designates the point at which the MOSFET lies in its on-state and it responds in a predictable manner. The most important aspects of defining the on-state of the MOSFET lie within the threshold voltage V_{TH} .

3.2 MOSFET Testing

MOSFET's were tested using a HP Parametric workstation connected to a Hewlett-Packard 4155A Semiconductor Parameter Analyzer **Figure 3-8**. FET's



Figure 3-8 – HP Parametric workstation connected to a Hewlett-Packard 4155A Semiconductor Parameter Analyzer

were placed on a grounded conducting platter and Source, Drain, and Gate Contacts were made via micromanipulators **Figure 3-9**. Ground contact was

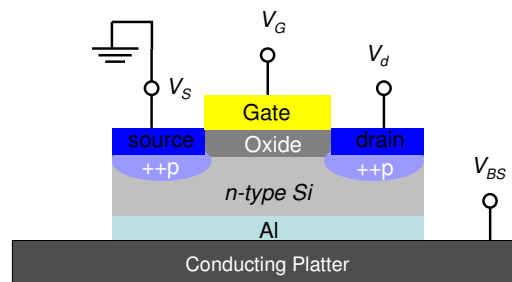


Figure 3-9 – Schematic of connections to FET from grounded conducting platter, Source, Drain, and Gate contacts were made via micromanipulators

made via a micromanipulator connected to the conducting platter. IV curves for the FET's were attained by applying a constant bias on the gate electrode V_G while sweeping the source and drain bias V_D . Monitoring of the source-drain current I_D initially exhibits a linear line with slope of approximately zero signifying

the off region of the FET. The V_G is then increased and the experiment is repeated. Plotting of the I_D vs V_D at specific V_G will reveal a host of IV curves. At lower V_G the I_D will be linear with a slope of approximately zero signifying that the FET is in its off-state. At large enough V_G the FET will exhibit a linear increase with a slope not equal to zero. This region referred to as the linear region is the on-state where charge is formed in the channel region of the FET that is opposite in charge to that of the applied V_G . The formed channel allows the shuttling of current between the source and drain electrodes I_D . As the V_D get larger, the I_D will level off and exhibit a region where the slope is approximately zero. This flat region is referred to as the saturation region and is due to the pinching-off of the channel due to the high drain bias V_D **Figure 3-10**.

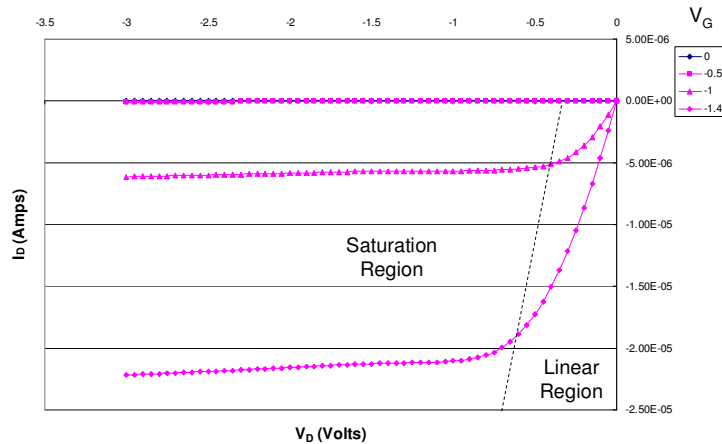


Figure 3-10 – I_D vs V_D curves at various V_G

The value we have interests in is the V_{TH} , the voltage at which the FET switches to its on-state. The V_{TH} can be more readily realized when plotting the I_D vs V_G at a given V_D that lies within the linear region of the FET. The ideal

value for V_D should be done at potentials used in sensing applications. Plots of the I_D vs V_D initially exhibit a linear response in the I_D with a slope near zero. At the point where the FET switches on, the plot exhibits a linear rise with a non-zero slope. Back-extrapolation of this value back down to where it crosses the zero slope region is the V_{TH} .

Performance of the FET was determined by making repeated measurements over several days. Bare FETs that exhibit less than 5% changes from day to day sampling were used as candidates for sensor applications.

Threshold Voltage Alteration

The V_{TH} is defined as being dependent on the flat band potential V_{FB} , strong inversion $2\psi_B$, and characteristics due to the substrate Equation 3-2.

$$V_{TH} \approx V_{FB} + 2\psi_B + \frac{\sqrt{2\epsilon_s q N_A (2\psi_B + V_{BS})}}{C_o} \quad \text{Equation 3-2}$$

Importantly the substrate characteristics also incorporate a substrate bias V_{BS} , that can be used to influence V_{TH} by pushing charges into the channel. Adjustments of the substrate biasing have been used to characterize MOSFETs.

Our interest is primarily the V_{FB} because it incorporates the work function Φ_{MS} between the gate and the substrate. V_{FB} is defined by the work function as well as charges within the oxide layer Equation 3-3. It has been shown that Φ_{MS}

$$V_{FB} = \Phi_{MS} - \frac{(Q_i + Q_{ox})}{C_o} \quad \text{Equation 3-3}$$

is primarily influenced by the work function of the metal Φ_M itself but also incorporates the influence due to the surface charge

3.3 SAM Formation

The formation of SAMs was first observed by Zisman³ but it wasn't until Nuzzo and Allara⁴ showed that SAMs can be readily formed from dilute solution of alkane thiols that the field really took off. Since then the formation of monolayers via a self assembly mechanism has expanded to a wide variety of applications.

SAMs are composed of molecular assemblies formed by adsorption of a surfactant onto a surface. Their self assembly makes them relatively easy to produce and attractive for building more complex 2D lattices. The relative ease and stability of SAM formation also makes them ideal candidates for surface modification studies. The most commonly researched SAMs are based on alkylthiols. In general the stability of the alkylthiol SAMs increases as the alkyl chain length increases due to van der Waals interactions⁴. Further modification of the alkyl chains leads to various packing efficiencies due to steric effects. Since then there has been an explosion in the research of SAMs and their potential applications.

One of the most studied aspects of SAMs is its electronic interaction with the substrate. Straight chained alkylthiol SAMs effectively act as an insulating layer between the metal substrate it is bound to and whatever conducting probe is used to make the electrical measurement. The insulating nature of a straight chained alkane is primarily due to the lack of an electron charge transport mechanism within the molecule. It has also been shown that aromaticity due to π

-bonds facilitate the transfer of charge across a molecule. It is through these studies that further research into the electronic character of SAMs on metal surfaces became warranted. One such important characteristic is surface potential that is a result of a combination of individual molecular dipoles acting as a 2-D array of molecular dipoles. Surface potentials of SAMs have been demonstrated to correlate with the dipole moments of the individual molecules.

3.3.1 SAM Formation leads to a Surface Potential

Kelvin Probe Microscopy has been used to show that the orientation of a SAM attached to a surface results in the formation of a sheet of dipoles⁵. Using various straight chained alkane thiols, the resulting surface potential arising from the orientation of dipoles on the surface has been shown to vary depending on chain length of the alkane. The chain length changes the effective dipole by increasing the distance between the negatively charged thiol head group and the positively charged alkane tail.

Further work has shown that changing the end group of the alkylthiols from a $-\text{CH}_3$ group to a $-\text{CF}_3$ group effectively flips the surface dipole^{6, 7}. Attachment of a highly electronegative trifluoro- group on the end of an alkylthiol results in a dipole where the electronegativity predominately resided at the much more electronegative trifluoro end than the thiol end. This leads to a dipole where the negative charge resides more on the trifluoro end than the thiol end. Surface attachment of trifluoro terminated alkane thiols exhibit surface potentials of opposite charge as compared to comparable methyl terminated alkylthiols.

Work on measuring the surface potential has also been expanded to SAM's of arylthiols. Through the use of conducting probe microscopies, the surface potential of various arylthiols was able to be measured. Some have shown that p-substituted arylthiols have shown that changing the electronegativity of the p-substituted group effectively changes the surface potential due to the electron withdrawing or electron donating character of the p-substituted group⁸.

Others have shown changes in surface potential due to other changes in substitution on the aryl ring⁹. They have also attempted to model the surface potential V_{sam} via individual molecular dipoles of the SAM arises as a result of a uniform 2-D array of dipoles Equation 3-4.

$$V_{sam} = \frac{N_{mol}(\vec{p} \cdot \vec{n})}{2K\epsilon_0} \quad \text{Equation 3-4}$$

Where p is the dipole per unit molecule, n is the unit vector normal to the surface, K is the dielectric constant of the molecular monolayer and ϵ_0 is the permittivity of space. The surface potential is then estimated from the amount of surface coverage N_{mol} and the approximate dipole moment of the molecule.

Since it is possible to chemically alter the work function Φ_M of the metal gate via SAM formation it may also be possible to further detect changes in the work function by simple modification of the SAM adhered to the metal gate. Alteration of the Φ_M will lead to changes in the flat band potential that can be monitored by shifts in the V_{TH} . We intend to use this in order to develop a

chemically gated sensing device based on a MOSFET platform. Comparison of the V_{TH} shift on a MOSFET before and after SAM formation will reveal alterations of the Φ_M in which we are interested in correlating to various SAM's.

Our research into the development of a chemically gated field effect transistor begun with a qualitative study of the response of fabricated MOSFET's to p-substituted phenylene isocyanides. Our use of phenylene isocyanides rather than benzylthiolates is due to the assumption that increased conjugation leads to better communication between the SAM and the Metal substrate.

Since we had yet to develop our surface potential capabilities, we depended on our general knowledge of chemical substitution on a phenylene ring just to see a general trend in the expected MOSFET response to SAM adsorption on the gate electrode. We were interested in seeing the MOSFET's response based on various p-substituted phenylene isocyanides. Knowing that nitro and isocyanide groups are electron withdrawing, and that alkyl, methoxy, and amino groups are electron donating to the phenylene rings **Figure 3-11** we expected to see

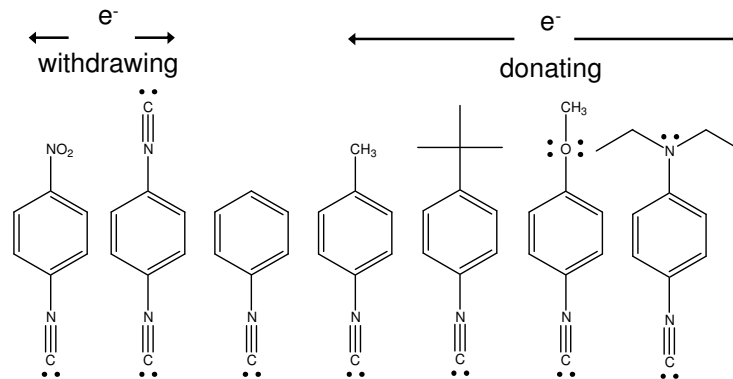


Figure 3-11 – *p*-substituted phenyl isocyanides

a change in the MOSFET's response depending on the substituted phenyl ring bound to the gate electrode. We expect to see a measurable shift in the V_{TH} that will correlate to the electron donating or withdrawing nature of the *p*-substituted ring as compared to the bare MOSFET.

In the case of the electron withdrawing *p*-substituted phenylene isocyanide we would expect V_{TH} to increase. This is due to the electron withdrawing phenylene isocyanide resulting in an effective positive biasing on the gate **Figure 3-12**. The

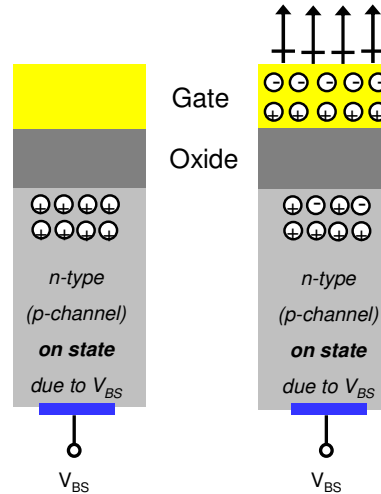


Figure 3-12 – Effect of gate biasing due to SAM formation of an e^- withdrawing molecules bound to surface

positive biasing of the gate in turn pulls more electrons into the channel. Since the FET is a p-channel FET, addition of electrons into the channel impede the flow of charge carriers, holes, thereby increasing the V_{TH} .

In the case of the electron donating p-substituted phenylene isocyanide we would expect V_{TH} to decrease. This is due to the electron donating phenylene isocyanide adding charge to the gate electrode, resulting in an effective negative biasing on the gate **Figure 3-13**. The negative biasing of the gate in turn pulls

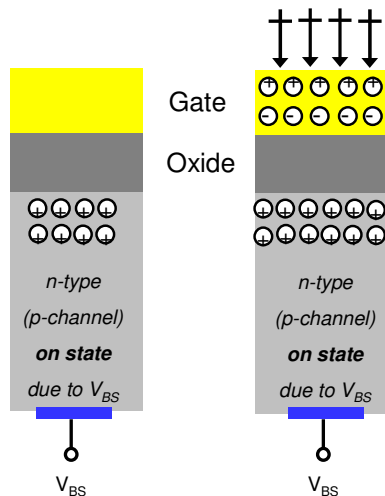


Figure 3-13 – Effect of gate biasing due to SAM formation of an e^- donating molecules bound to surface

more holes into the channel thereby increasing number of charge carriers. The increase of charge carriers within the gate should result in a decrease in the V_{TH} .

3.4 Experimental

Phenylene isocyanide and p-methoxy-phenylene isocyanide were purchased from Acros and used as received with no further purification necessary. 1,4-Phenylene diamine, p-nitro aniline, p-tert-butyl aniline, p-methyl aniline, p-diethylamino aniline were purchased from Aldrich used as received with no further purification. All solvents were purchased from Aldrich and were HPLC grade.

1,4-Phenylene Diisocyanide: 1,4-phenylene diamine (5.316g, 25mmol) was suspended in 60ml dichloromethane (CH_2Cl_2) and stirred. 2.6 equivalents of chloroform (CHCl_3) (3.8g, 32.5mmol) were added to the suspension followed by addition of benzyltriethylammonium chloride (.500g), a phase transfer catalyst. A 50% sodium hydroxide (NaOH) solution (60mL) was added and the system was allowed to reflux for 4 hours. The system was quenched by addition of 50 mL of deionized (DI) water. The resulting reaction formed a brown mixture that was transferred to a separatory funnel and diluted with 50mL CH_2Cl_2 . The organic phase was washed with 2 x 100 mL DI water and 100 mL saturated NaCl solution then before being separated and dried over magnesium sulfate. The solvent was removed in a rotary evaporator leaving a tan solid that was purified on a column of alumina with a 3:1 mixture of hexanes:ethyl acetate. Evaporation of the eluate gave a white solid (42% yield). IR spectrum (KBr): $\nu(\text{N}\equiv\text{C})$ 2135 cm^{-1} . $^1\text{H-NMR}$ (CDCl_3 , 300 MHz) δ [ppm]: 7.418 (s, ArH).

p-Nitro Phenylene Isocyanide: p-Nitro phenylene isocyanide was synthesized from p-nitroaniline with the same methods used to synthesize 1,4-phenylene

diisocyanide with the exception of using only 1.3 equivalents of CHCl_3 . p-Nitro phenylene isocyanide yield = 54% (yellow solid).

p-tert-butyl-Phenylene Isocyanide : p-tert-butyl-phenylene isocyanide was synthesized from p-tert-butyl aniline with the same methods used to synthesize 1,4-phenylene diisocyanide with the exception of using only 1.3 equivalents of CHCl_3 . p-tert-Butyl-phenylene isocyanide yield = 33% (white solid).

p-Methyl Phenylene Isocyanide: p-Methyl phenylene isocyanide was synthesized from p-methyl aniline with the same methods used to synthesize 1,4-phenylene diisocyanide with the exception of using only 1.3 equivalents of CHCl_3 . p-Methyl phenylene isocyanide yield = 28% (off-white solid).

p-Diethyl Amino Phenylene Isocyanide: p-Diethyl amino phenylene isocyanide was synthesized from p-diethylamino aniline with the same methods used to synthesize 1,4-phenylene diisocyanide with the exception of using only 1.3 equivalents of CHCl_3 . p-Diethyl amino phenylene isocyanide yield = 37% (light green solid). IR spectrum (KBr): $\nu(\text{N}=\text{C})$ 2158cm^{-1} . $^1\text{H-NMR}$ (CDCl_3 , 400 MHz) δ [ppm]: 1.02 (t, 6H, CH_3), 3.02 (q, 4H, CH_2), 6.22 (s, 2H, ArH).

Phenylene Isocyanide: Phenylene isocyanide was used as purchased from Aldrich. No further purification was used. Phenylene isocyanide (off-white solid). IR spectrum (KBr): $\nu(\text{N}=\text{C})$ 2154 cm^{-1} .

SAMs of the various phenylene isocyanides were prepared by using 10mM solutions of the above molecules prepared in dry CH_2Cl_2 from the lab solvent system. MOSFETs were soaked for several days and then rinsed in dry CH_2Cl_2 and blown dry with N_2 . Parallel surface analysis studies on Au coated

silicon wafers prepared exactly the same as the gate electrodes were done due to the gate electrodes on the MOSFETs being too small for surface analysis. Surface IR studies were done using a Bruker Equinox 55 FT-IR mated with a Bruker PMA-35 attachment for PM-IRRAS measurements. SAM thickness was measured using a Gaertner Ellipsometer. Threshold voltages were measured using a HP Parametric workstation connected to a Hewlett-Packard 4155A Semiconductor Parameter Analyzer.

3.5 Surface IR/SAM Formation

Out of the seven possible phenylene isocyanide molecules attempted only three of the molecules formed well behaved SAMs p-diethylamino-phenylene isocyanide, p-phenylene diisocyanide, and phenylene isocyanide with the observed C-N stretching frequencies **Table 3-1**. Comparison of the isocyanide stretch of free

Table 3-1 - C-N Stretching Frequencies for various Phenyl Isocyanide SAMs

	KBr	SAM	
	C-N Stretch	Surface Bound C-N Stretch	Free C-N Stretch
phenyl isocyanide	2154	2230	
1,4-phenyl diisocyanide	2135	2185	2121
p-diethylamino phenyl isocyanide	2158	2197	

phenylene isocyanide (2154cm^{-1}) versus the surface bound phenylene isocyanide (2230cm^{-1}) shows a shift in the isocyanide adsorption peak **Figure 3-15**. This shift is attributed to back bonding from the surface to the phenylene isocyanide SAM. The narrowness of the isocyanide peak for the surface bound SAM suggests that the SAM is a very well organized monolayer.

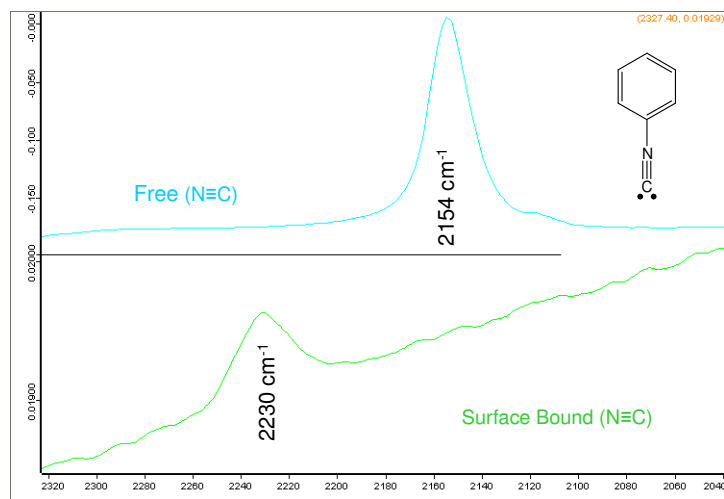


Figure 3-15 – IR stretch for free phenyl isocyanide (top) vs surface bound phenyl isocyanide (bottom)

Surface IR measurements of the p-phenylene diisocyanide from the PM-IRRAS exhibited an IR peak corresponding to two different isocyanide stretches at 2185cm^{-1} and 2121cm^{-1} **Figure 3-16**. The two different IR stretches correspond to the differences in the orientation of the isocyanide groups. The free isocyanide is the peak at 2121cm^{-1} , leaving the peak at 2185cm^{-1} to be the isocyanide group bound to the surface.

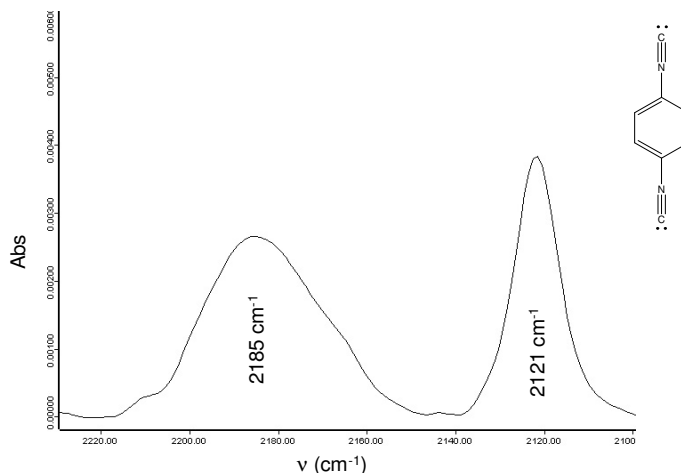


Figure 3-16 – IR stretches of free isocyanide (2121cm⁻¹) and surface bound isocyanide (2185cm⁻¹) peaks for 1,4-phenyl diisocyanide

V_{TH} Shift

Testing of the coated FETs was done in the same manner as that of a bare MOSFET with the exception of the fact that no electrode contact to the coated gate was made. Electrical contacts to the source and drain electrodes were achieved by burying the electrodes into the surface of the source and drain electrodes.

Out of the three different well ordered SAMs (p-diethylamino-phenylene isocyanide, p-phenylene diisocyanide, and phenylene isocyanide) only two of the samples resulted in the consistent V_{TH} shifts the p-diethylamino-phenylene isocyanide and the p-phenylene diisocyanide SAMs. The phenylene isocyanide FET was determined to be unstable and removed from the study.

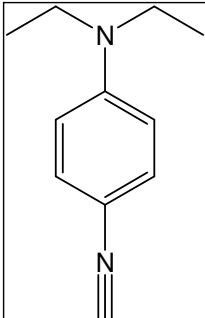
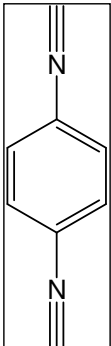
V_{TH} is indirectly correlated to the I_{DS} in the saturation region of the FET

Equation 3-5. Comparison of the IV curves at $V_{BS} = 1.0V$ of the p-substituted

$$I_{DS} = \frac{W}{2L} C_{ox} \bar{\mu}_n (V_G - V_T)^2 \quad \text{Equation 3-5}$$

phenylene isocyanides SAM vs the bare FET with $V_G=0$ were made and shifts in the I_{DS} are observed. The p-diethylamino-phenylene isocyanide exhibits a $\Delta I_{DS} = -10\mu\text{A}$. The p-phenylene diisocyanide exhibits a $\Delta I_{DS} = +50\mu\text{A}$. Due to the lack of surface potential measurements the magnitude of the measured shifts cannot be quantitatively assessed. Qualitatively the measured ΔI_{DS} correlates to the expected V_{TH} shifts and are summarized in **Table 3-2**.

Table 3-2 - Measured I_{DS} , and V_{TH} shifts due SAM formation on gate electrode

Molecule	ΔI_{DS}	V_{TH} Shift
	Electron Donating +50 μA	↓
	Electron Withdrawing -10 μA	↑

REFERENCES

1. Wanlass, F. M.; Sah, C. T., Nanowatt Logic Using Field-Effect Metal-Oxide Semiconductor Triodes. *International Solid State Circuits Conference Digest of Technical Papers* **1963**, 32-33.
2. Moore, G., Cramming More Components onto Integrated Circuits. *Electronics Magazine* **1965**, 38, (8).
3. Bigelow, W. C.; Pickett, D. L.; Zisman, W. A., *J. Colloid Interface Sci* **1946**, 1, 513.
4. Nuzzo, R. G.; Allara, D. L., *J. Am. Chem. Soc.* **1983**, 105, 4481.
5. Evans, S. D.; Ulman, A., Surface Potential Studies of Alkyl-thiol monolayers adsorbed on Gold. *Chemical Physics Letters* **1990**, 170, (5,6), 462-466.
6. Alloway, D.; Hofman, M.; Smith, D.; Gruhn, N.; Graham, A.; Colorado, R.; Wysocki, V.; Lee, T. R.; Lee, P. A.; Armstrong, N. R., Interface Dipoles Arising from Self-Assembled Monolayers on Gold: UV-Photoemission Studies of Alkanethiols and Partially Fluorinated Alkanethiols. *Journal Physical Chemistry B* **2003**, 107, 11690-11699.
7. Rusu, P.; Brocks, G., Surface Dipoles and Work Functions of Alkylthiolates and Fluorinated Alkylthiolates on Au(111). *Journal Physical Chemistry B* **2006**, 110, 226828-22634.
8. Zehner, R.; Parsons, B.; Hsung, R.; Sita, L., Tuning the Work Function of Gold with Self-Assembled Monolayers Derived from X-[C₆H₄-C=C-]_nC₆H₄-SH (n=0,1,2:H,F,CH₃, CF₃ and OCH₃). *Langmuir* **1999**, 15, 1121-1127.
9. Howell, S.; Kuila, D.; Kasibhatla, B.; Kubiak, C. P.; Janes, D.; Reifenberger, R., Molecular Electrostatics of Conjugated Self-Assembled Monolayers on Au(111) Using Electrostatic Force Microscopy. *Langmuir* **2002**, 18, 5120-5125.

Chapter 4

Sensor Development Using Interdigitated Electrodes

4.1 Introduction

Our interests in the development of chemical sensing elements activated by a chemical binding event was expanded into the detection of glucose and other diol molecules such as carbohydrates after discovering articles from Professor Bakthan Singaram. His research group was involved in the use of phenyl boronic acid derivatives for optical detection of glucose and other carbohydrates¹⁻³. They have synthesized derivatives of viologen with boronic adducts. Using a two component system, substituted viologen and a fluorescent dye such as pyranine, they have shown that it is possible to optically detect the presence of glucose by fluorescence.

Originally, others have shown that a fluorescent dye such as 8-hydroxy-1,3,6-pyrenestrifonic acid (HPTS), in the presence of viologen and substituted viologens, will quench the fluorescence of the dye⁴.

Singaram expanded this work to larger viologens such as a *m*-benzyl boronic viologen (*m*-BBV). They have shown that the HPTS fluorescence is

quenched in the presence of *m*-BBV due to the formation of a complex between the two. Upon exposure to carbohydrates such as glucose, the fluorescence returns suggesting that the complex formation between the HPTS and *m*-BBV is disrupted by binding to the carbohydrates² **Figure 4-1**.

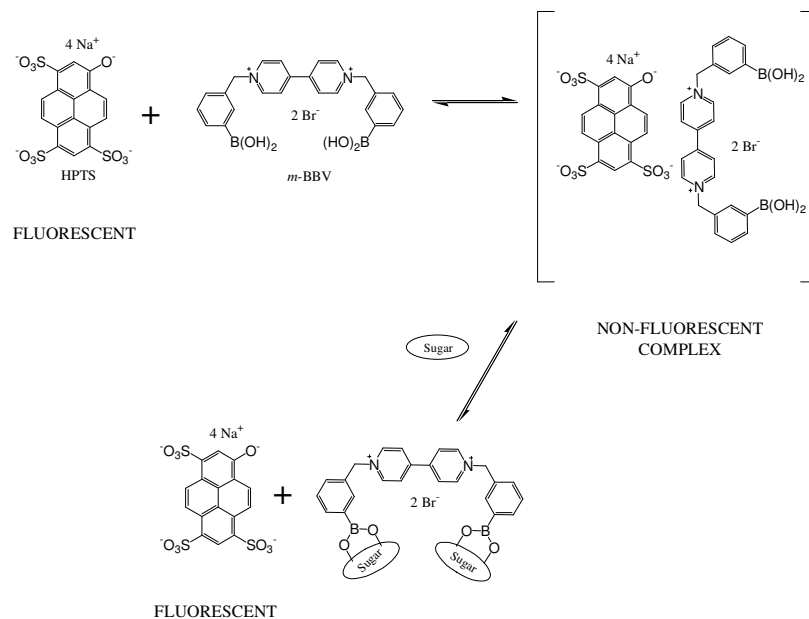


Figure 4-1 – Formation of two component non-fluorescent binding complex of [HPTS - *m*-BBV]. Sugar binding to the *m*-BBV results in increased fluorescence due to decrease in the amount of [HPTS-*m*-BBV].

In looking at this system we realized that binding of the sugars to the boronic acids changes the molecule's ability to form the complex resulting in free HPTS to fluoresce. We thought that it would be possible to use this knowledge and apply it to other systems. Ideally we were interested in finding a boronic acid system that we could use within a direct, non-optical sensing platform such as interdigitated electrodes.

Recently there has been work done on polymerizable boronic acid systems such as poly aniline boronic acid⁵ that rely on potentiometric measurements to measure the binding of glucose. Shoji has also been working with polyaniline boronic acids for the purpose of glucose detection⁶. They were able to show that they could potentiometrically quantify the amount of binding based on the ratio of glucose stabilized benzyl diamine versus quinone diimine **Figure 4-2**.

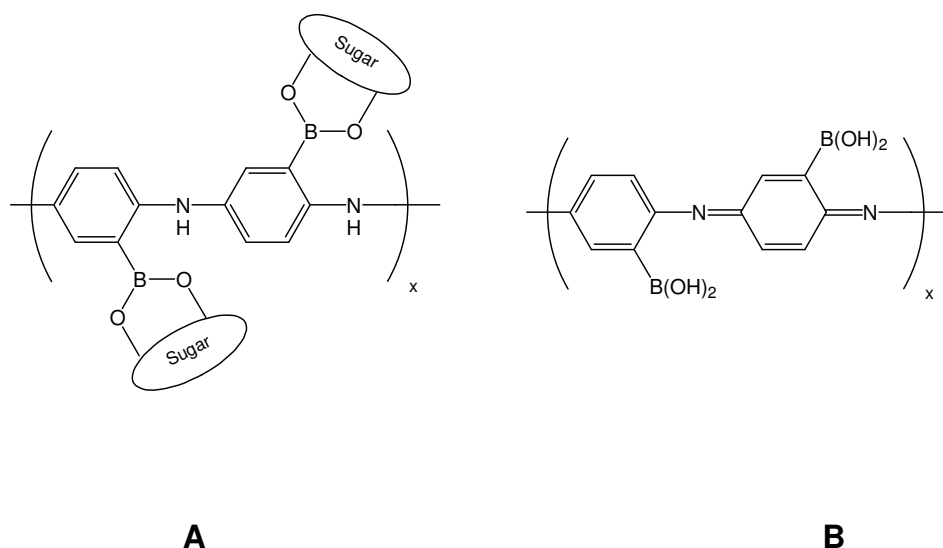


Figure 4-2 – Stabilized benzyl diamine via sugar binding (A) vs quinone diimine (B)

We seek to expand this field by investigating the feasibility of using thiophene-3-boronic acid as a polymerizable system for the detection of glucose. In order to do so, we show that thiophene-3-boronic will readily bind to glucose. We also show x-ray crystallography data that confirms the binding of the sugars to the boronic acid moiety is by boronic ester linkages. And finally, we show that

we obtain an electrical response upon addition of glucose to the thiophene boronic acid that has been polymerized across interdigitated electrode arrays.

4.2 Thiophene-3-Boronic Acid Binding Study

The nature of the boronic acid-diol interaction was not understood until recently⁷. The binding of diols to boronic acid results in the formation of a boronate ester that is both pH and solvent dependent. In the present work, we report the binding of glucose and fructose to thiophene-3-boronic acid (TBA). This interaction was probed via competitive binding experiments with the fluorescence sensitive Alizarin Red S. (ARS) The fluorescence quenching of the diol Alizarin Red S is due to an excited state proton transfer from the phenol hydroxyl group to the ketone oxygen.⁸ Binding of a boronic acid to the phenyl hydroxyl groups of the Alizarin Red S will form a boronate ester. The boronate ester eliminates the molecule's ability to self quench **Figure 4-3** which results in an increase in fluorescence

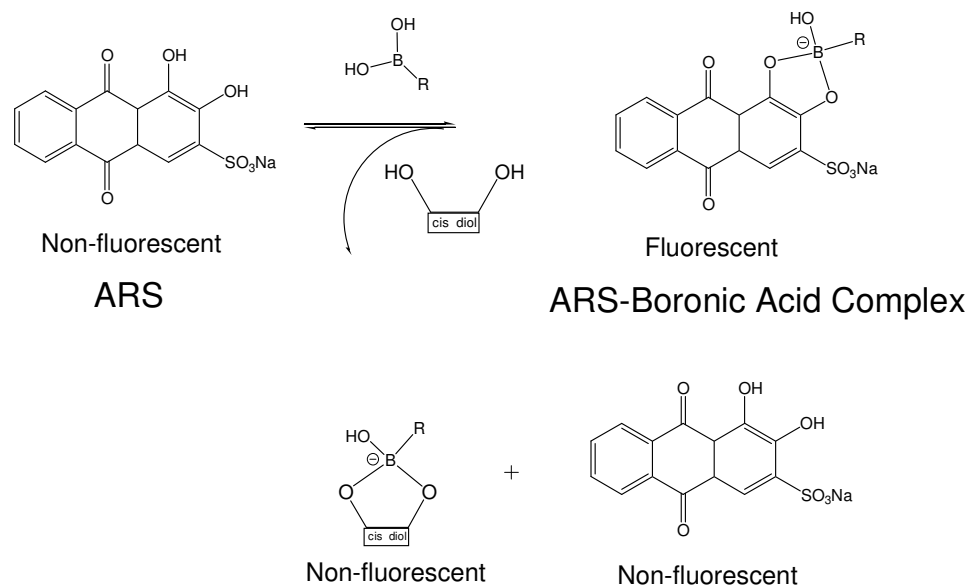


Figure 4-3 – Three component competitive binding scheme. Binding of diols to the boronic acid prevents formation of fluorescent ARS-Boronic Acid Complex

yield⁹⁻¹¹. The fluorescence study will provide insight into the equilibrium processes between diols and boronic acids.

The fluorescence of a three component competitive binding interaction between a sugar, ARS, and thiophene-3-boronic acid, was monitored by observing the formation of Alizarin Red S - thiophene-3-boronic acid complex (ARS-TBA). The addition of glucose or other diols to the system compete for the binding position of the ARS via formation of a Diol - Thiophene-3-Boronic Acid complex (Diol-TBA). The competitive binding experiments then allow determination of various thiophene-3-boronic acid-diol binding constants.

The degree of complexation of the thiophene-3-boronic acid-Alizarin Red S complex was determined using fluorescence spectroscopy at room temperature. The spectra were determined by exciting the complex with an absorption peak at 517nm and monitoring a fluorescence emission peak at

570nm. The fluorescence emission spectra of the ARS-TBA complex exhibit the expected linear response to increased [TBA] followed by saturation as the [TBA] > [ARS] **Figure 4-4**. The three component complexation study of thiophene-3-boronic acid and ARS was performed with glucose and fructose.

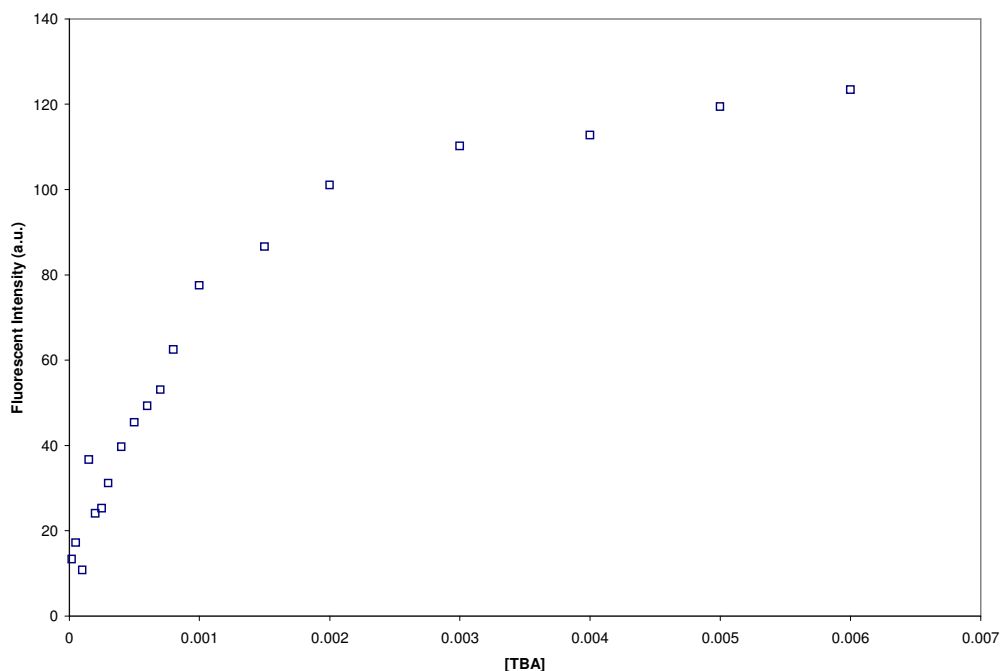


Figure 4-4 – Relative fluorescence versus the [TBA] at constant [ARS]. Graph shows characteristic fluorescence response to increasing [ARS]. (□ actual data)

A Job Plot of the Alizarin Red S. – thiophene-3-boronic acid complex (ARS-TBA) was obtained by mixing various ratios (Total concentration = 100 μ M) of Alizarin Red S. to thiophene-3-boronic acid in the pH 7.4 buffer. The Job plot showed a 1:1 ratio of the Alizarin Red S to thiophene-3-boronic acid Figure 4-5.

The 1:1 ARS:TBA ratio allows us to use the Benesi-Hildebrand method¹² for determination of the equilibrium constants.

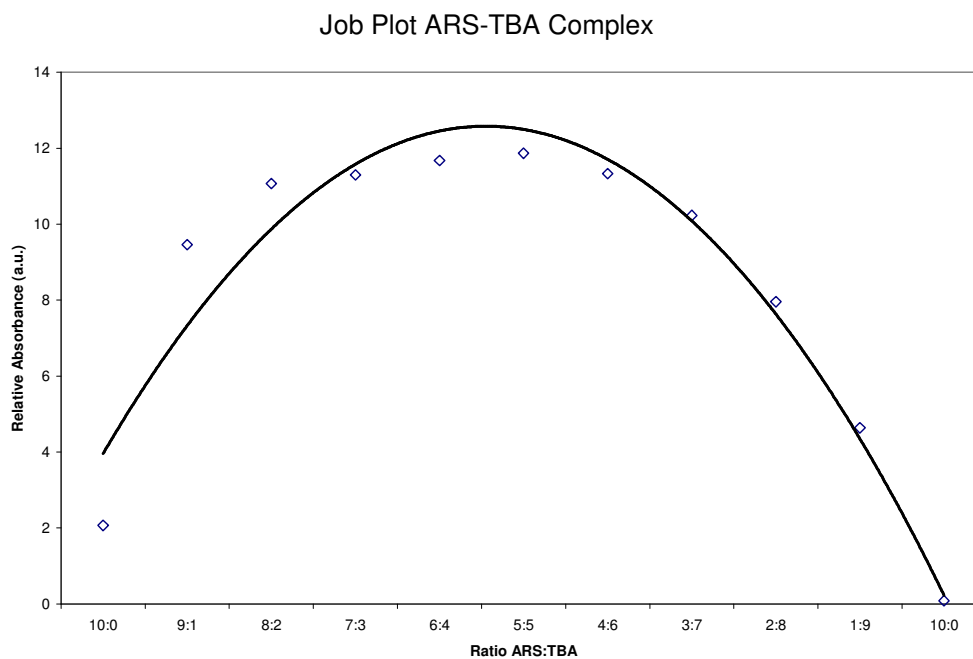


Figure 4-5 – Job Plot binding of ARS/TBA scheme. Plot shows that there is preferential 1:1 binding between ARS:TBA. (\diamond actual data, — is best fit line)

Quantification of the amount of ARS-TBA complexation was determined by titrations of TBA acid with various amounts of ARS. By maintaining a large excess of the TBA as compared to the ARS (10x – 1000x), it can be assumed that the equilibrium was shifted towards the product side such that the initial amount of Alizarin Red S. is equal to the amount of complex formed. The plot of the amount of relative fluorescence versus the [ARS-TBA] shows linear characteristics and is used as the calibration curve for determining the

concentration of ARS-TBA complex formed throughout all experiments **Figure 4-**

6.

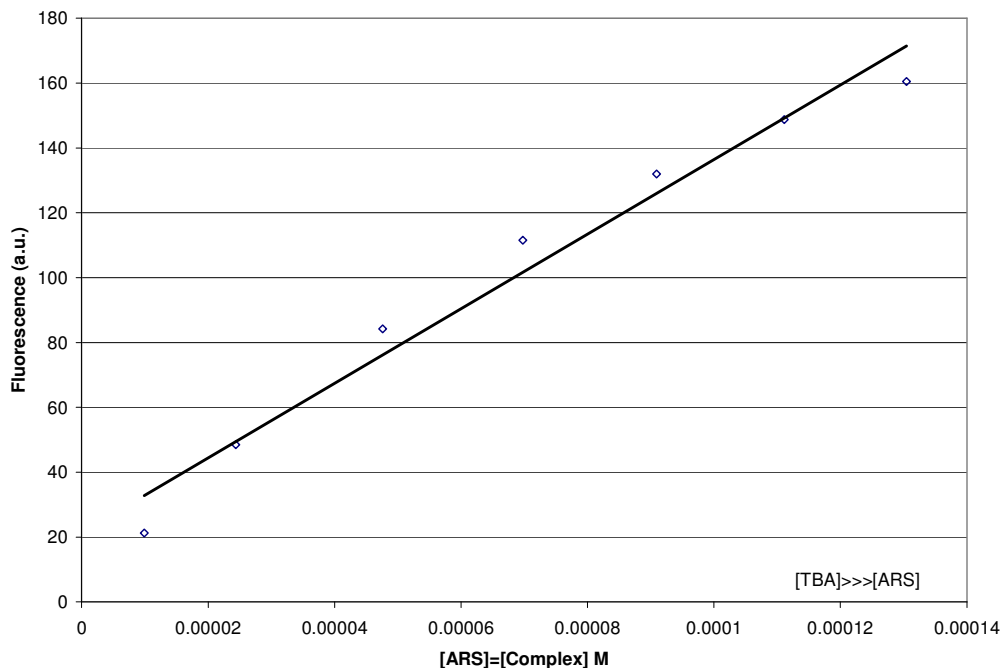


Figure 4-6 – Relative fluorescence versus the [ARS] shows linear response [ARS]. Since $[TBA] \gg [ARS]$ it is assumed that all ARS has formed [ARS-TBA] complex thus allowing calibration for determining the concentration of ARS-TBA complex formed throughout all experiments (\diamond actual data, — is best fit line $R^2 = .9722$)

By holding the concentration of ARS constant and varying the concentration of the TBA the amount of complex formed is determined using the measured fluorescence. The amount of complex formed is also used in determining the amount of free TBA ($TBA_{unbound}$) by the difference between the initial amount of TBA and the amount of complex formed.

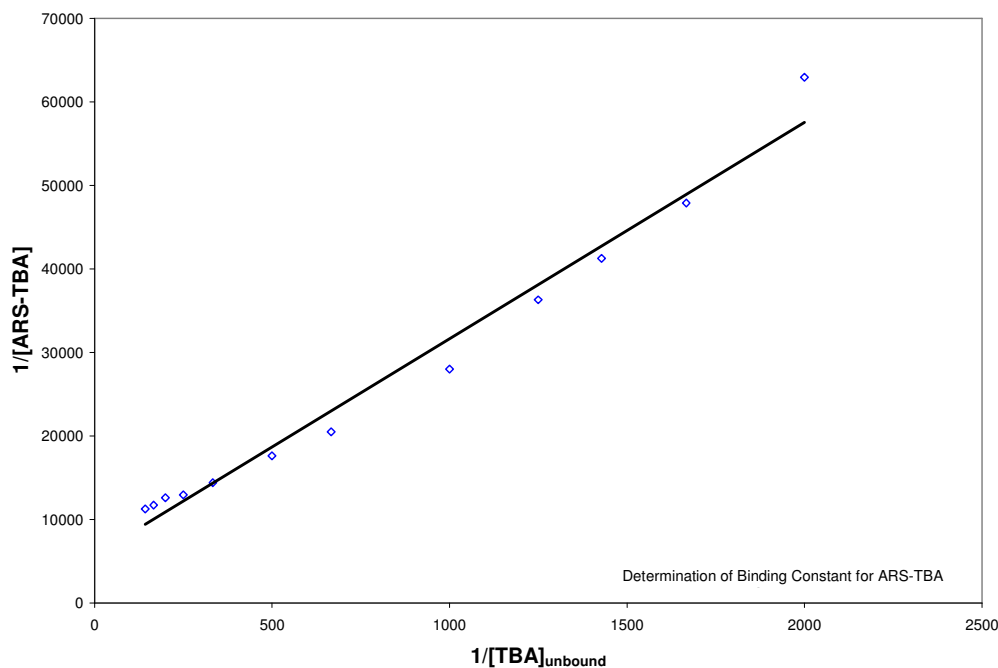


Figure 4-7 – $1/[\text{ARS-TBA}]$ vs $1/[\text{TBA}]_{\text{unbound}}$ allows for determination of K_{eq} for $[\text{ARS-TBA}]$ (\diamond actual data, — is best fit line $R^2=.9793$)

The plot of $1/[\text{ARS-TBA}]$ vs $1/[\text{TBA}]_{\text{unbound}}$ **Figure 4-7** has a linear relationship with the binding constant being determined from the slope, **Equation 4-1**.

$$\text{SLOPE} = \frac{1}{K_{\text{eq}}[\text{ARS}]_o} \quad (\text{Equation 4-1})$$

The binding constant determination of the other diols to the TBA is done via titration of a constant $[\text{ARS}]_o$ and $[\text{TBA}]_o$ with various concentrations of diol. Addition of the diol results in a decrease in the $[\text{ARS-TBA}]$ measured fluorescence. The decrease is due to a shift in the equilibrium due to the formation of a $[\text{Diol-TBA}]$ complex which results in the liberation of free ARS that does not exhibit fluorescence. Thus the amount of change in the fluorescence is proportional to the amount of $[\text{Diol-TBA}]$ formed. Calculation of the

formation constant (K_{eq_2}) for the formation of the Diol-TBA complex was done via Wang's method⁷. In the case of addition of various concentrations of glucose, the K_{eq_2} is calculated from the plot of $1/P$ vs Q (**Figure 4-8**) using the relation **Equation 4-2** where K_{eq_1} is the binding constant for the formation of the [ARS-TBA].

$$\frac{[Diol]_o}{P} = \frac{K_{eq_1}}{K_{eq_2}} Q + 1 \quad (\text{Equation 4-2})$$

P is defined by **Equation 4-3**

$$P = [TBA]_o - \frac{1}{QK_{eq_1}} - \frac{[ARS]_o}{Q+1} \quad (\text{Equation 4-3})$$

Q is defined by **Equation 4-4**

$$Q = \frac{[ARS]}{[ARS - TBA]} \quad (\text{Equation 4-4})$$

The plot (**Figure 4-8 and 4-9**) depicts a linear relation where the K_{eq_2} is derived from the slope of the line divided by K_{eq_1} , as determined by **Equation 4-2**.

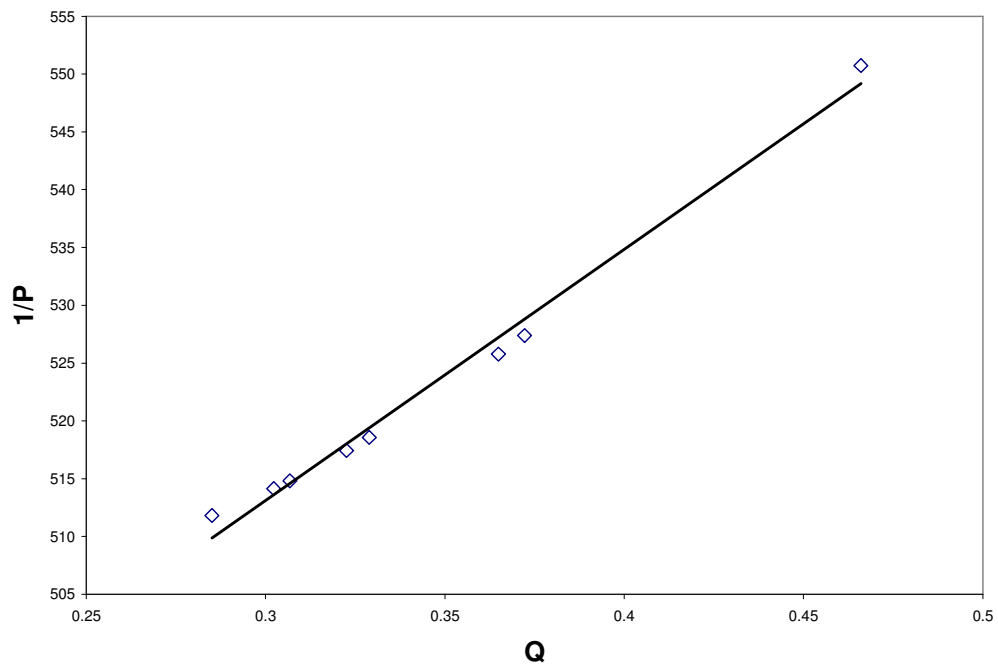


Figure 4-8 – $1/P$ vs Q for Determination K_{eq} Glucose Slope = 217.26 (\diamond actual data, — is best fit line $R^2=.9896$)

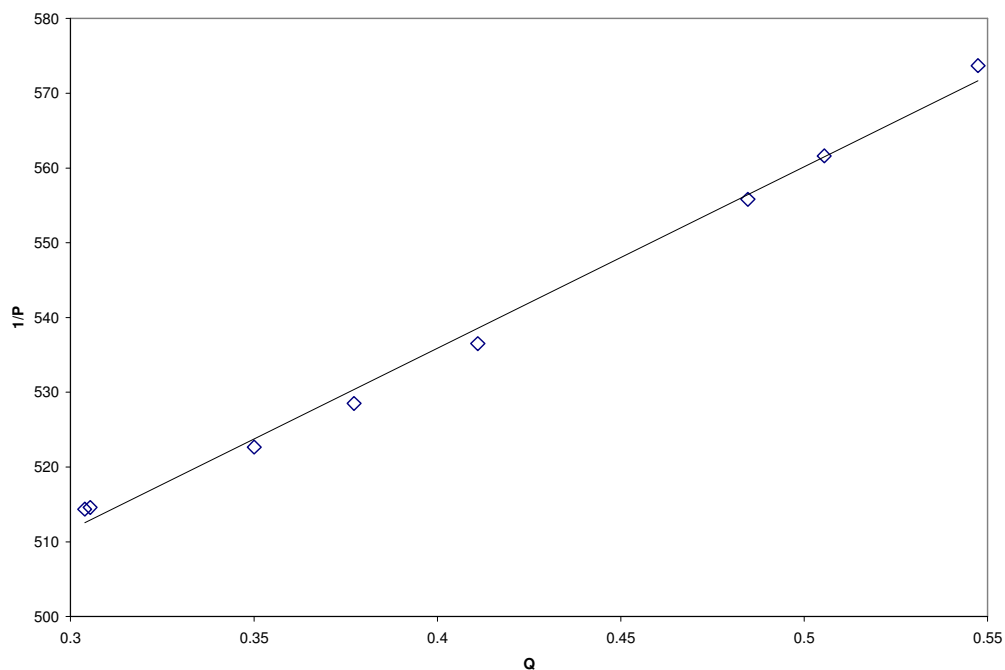


Figure 4-9 – $1/P$ vs Q for Determination K_{eq} Fructose Slope = 242.75 (\diamond actual data, — is best fit line $R^2=.9945$)

Using the ARS fluorescence method, the binding constants of ARS **Figure 4-7**, glucose **Figure 4-8** and fructose **Figure 4-9** with thiophene 3-boronic acid were determined at pH 7.4 **Table 4-1**. The binding constants we report are similar to those found for other aryl boronic acid systems such as phenyl boronic acids. The ARS shows extremely high affinity for the thiophene-3-boronic acid with a K_{eq} value of 9010 M^{-1} .

Table 4-1 - Binding constants K_{eq} (M^{-1}) with thiophene-3-boronic acid in NPBS (pH

	K_{eq} (M^{-1})
ARS	9010 \pm 101
Glucose	42 \pm 0.1
Fructose	37 \pm 1.1

Fructose and Glucose have binding constants of 37 and 42 M^{-1} , respectively. The glucose binding constant for thiophene-3-boronic acid is an order of magnitude higher than the binding constant for phenyl boronic acid which was reported to be 4.6 M^{-1} ⁷.

The competitive binding study revealed that the binding constant of glucose to TBA is an order of magnitude larger than the binding to polyaniline boronic acid. This supports the probability in the development of a glucose sensor triggered by glucose binding to a polymerized thiophene boronic acid. Also, the higher binding to the TBA may allow for tunability of the binding via substitution on the TBA.

4.3 Preparation and X-Ray Crystallography of Thiophene Boronic Acid-Sugar Complexes

X-ray crystal structures of 4,4,5,5-tetramethyl-2-thiophene-3-yl-[1,3,2] dioxaborolane (complex **1**) and 2-thiophene-3-yl-[1,3,2] dioxaborolane (complex **2**) were completed to support the chemical binding of diols to thiophene-3-

boronic acid. The complex **1**, 4,4,5,5-tetramethyl-2-thiophene-3-yl-[1,3,2] dioxaborolane was prepared by dissolving pinacol and thiophene-3-boronic (1:1) acid in dry dichloromethane. The two solutions were mixed together and allowed to sit for days in a vial with a needle pierced septum to allow the solvent to slowly evaporate. After several days, white, needle crystals had formed at the bottom of the vial. X-ray crystallography confirmed that the binding of the pinacol to the thiophene-3-boronic acid **Figure 4-10** occurs *via* formation of a boronate ester complex. A similar study with 1,2-ethane diol and thiophene-3-boronic acid (1:1)

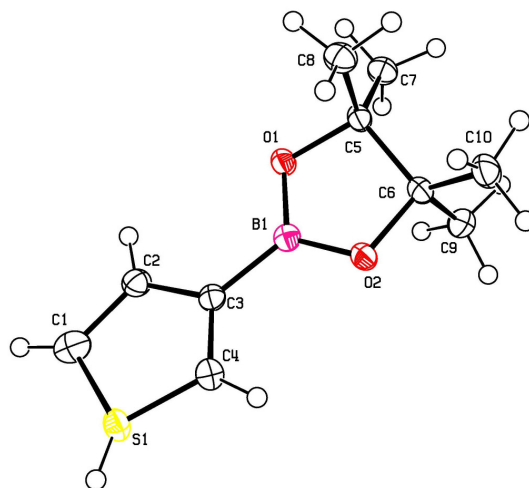


Figure 4-10 – X-ray crystal structure of 4,4,5,5-tetramethyl-2-thiophene-3-yl-[1,3,2] dioxaborolane, complex **1**, confirming the formation of the boronate-ester complex between pinacol and thiophene-3-boronic acid.

was performed in dichloromethane with the similar results forming 2-thiophene-3-yl-[1,3,2] dioxaborolane, complex **2**, after several days. White, needle crystals formed that exhibited a similar boronate ester complex as confirmed by x-ray crystallography **Figure 4-11**.

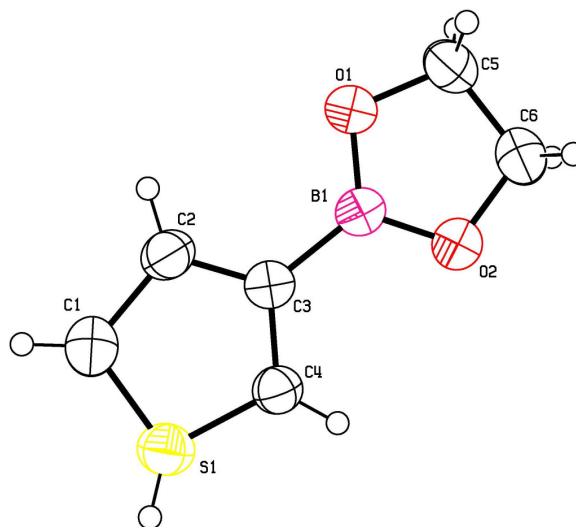


Figure 4-11 – X-ray crystal structure of 4,4,5,5-tetramethyl-2-thiophene-3-yl-[1,3,2] dioxaborolane, complex **2**, confirming the formation of the boronate-ester complex between 1,2-ethane diol and thiophene-3-boronic acid.

Structures of glucose with thiophene-3-boronic acid were also attempted but a crystal structure of the complex was not attainable. Many different solvents were used but it appears that the insolubility of the glucose in organic solvents to be the main issue even with refluxing of the solution mixtures.

Table 4-2. Crystal data and structure refinement for complex **1**.

X-ray ID	kub07a	
Sample/notebook ID	TBAPincol1	
Empirical formula	C ₁₀ H ₁₅ B O ₂ S	
Formula weight	210.09	
Temperature	100(2) K	
Wavelength	0.71073 Å	
Crystal system	Orthorhombic	
Space group	Pbca	
Unit cell dimensions	a = 13.879(2) Å	α = 90°.
	b = 12.2142(18) Å	β = 90°.
	c = 26.187(4) Å	γ = 90°.
Volume	4439.2(11) Å ³	
Z	16	
Density (calculated)	1.257 Mg/m ³	
Absorption coefficient	0.262 mm ⁻¹	
F(000)	1792	
Crystal size	0.70 x 0.40 x 0.02 mm ³	
Crystal color/habit	colorless plate	
Theta range for data collection	1.56 to 28.27°.	
Index ranges	-18 ≤ h ≤ 18, -16 ≤ k ≤ 15, -34 ≤ l ≤ 34	
Reflections collected	35944	
Independent reflections	5285 [R(int) = 0.0415]	
Completeness to theta = 25.00°	100.0 %	
Absorption correction	Semi-empirical from equivalents	
Max. and min. transmission	0.9948 and 0.8376	
Refinement method	Full-matrix least-squares on F ²	
Data / restraints / parameters	5285 / 0 / 263	
Goodness-of-fit on F ²	1.041	
Final R indices [I > 2σ(I)]	R1 = 0.0425, wR2 = 0.1054	
R indices (all data)	R1 = 0.0571, wR2 = 0.1138	
Largest diff. peak and hole	0.476 and -0.185 e.Å ⁻³	

Table 4-3. Atomic coordinates ($\times 10^4$) and equivalent isotropic displacement parameters ($\text{\AA}^2 \times 10^3$) for complex **1**. $U(\text{eq})$ is defined as one third of the trace of the orthogonalized U_{ij} tensor.

	x	y	z	U(eq)
C(1)	2379(1)	2614(1)	2361(1)	34(1)
C(1A)	2167(1)	3946(1)	2144(1)	23(1)
C(2)	2632(1)	1993(1)	1893(1)	24(1)
C(3)	2626(1)	2605(1)	1432(1)	19(1)
C(4)	2382(1)	3684(1)	1526(1)	22(1)
C(5)	2923(1)	891(1)	243(1)	20(1)
C(6)	3186(1)	2063(1)	43(1)	22(1)
C(7)	3632(1)	-1(1)	98(1)	24(1)
C(8)	1901(1)	539(1)	111(1)	26(1)
C(9)	4263(1)	2246(1)	-18(1)	29(1)
C(10)	2650(1)	2410(1)	-437(1)	30(1)
C(11)	189(1)	-573(1)	3573(1)	31(1)
C(11A)	200(1)	851(1)	3639(1)	27(1)
C(12)	1284(1)	-821(1)	3477(1)	24(1)
C(13)	1891(1)	107(1)	3487(1)	20(1)
C(14)	1357(1)	1059(1)	3571(1)	24(1)
C(15)	4528(1)	-628(1)	3386(1)	19(1)
C(16)	4561(1)	651(1)	3336(1)	21(1)
C(17)	4823(1)	-1040(1)	3914(1)	25(1)
C(18)	5075(1)	-1246(1)	2975(1)	26(1)
C(19)	5266(1)	1204(1)	3697(1)	31(1)
C(20)	4712(1)	1051(1)	2793(1)	31(1)
B(1)	2824(1)	2130(1)	893(1)	19(1)
B(2)	3003(1)	73(1)	3429(1)	20(1)
O(1)	2951(1)	1035(1)	800(1)	20(1)
O(2)	2866(1)	2767(1)	465(1)	23(1)
O(3)	3499(1)	-874(1)	3330(1)	21(1)
O(4)	3579(1)	975(1)	3484(1)	24(1)

Table 4-3. (cont.)

	x	y	z	U(eq)
S(1)	2167(1)	3946(1)	2144(1)	23(1)
S(1A)	2379(1)	2614(1)	2361(1)	34(1)
S(2)	200(1)	851(1)	3639(1)	27(1)
S(2A)	189(1)	-573(1)	3573(1)	31(1)

Table 4-4. Bond lengths [Å] and angles [°] for complex 1.

C(1)-C(2)	1.4818(18)	C(12)-C(13)	1.412(2)
C(1A)-C(4)	1.6761(14)	C(13)-C(14)	1.397(2)
C(2)-C(3)	1.4204(19)	C(13)-B(2)	1.550(2)
C(3)-C(4)	1.383(2)	C(15)-O(3)	1.4667(15)
C(3)-B(1)	1.552(2)	C(15)-C(18)	1.5179(19)
C(5)-O(1)	1.4698(16)	C(15)-C(17)	1.5261(19)
C(5)-C(7)	1.5161(19)	C(15)-C(16)	1.568(2)
C(5)-C(8)	1.5222(19)	C(16)-O(4)	1.4705(16)
C(5)-C(6)	1.5666(19)	C(16)-C(20)	1.518(2)
C(6)-O(2)	1.4686(16)	C(16)-C(19)	1.519(2)
C(6)-C(9)	1.519(2)	B(1)-O(2)	1.3660(18)
C(6)-C(10)	1.522(2)	B(1)-O(1)	1.3705(18)
C(11)-C(12)	1.5702(16)	B(2)-O(4)	1.3692(18)
C(11A)-C(14)	1.6361(15)	B(2)-O(3)	1.3712(18)
C(3)-C(2)-C(1)	115.63(12)	C(7)-C(5)-C(6)	114.94(11)
C(4)-C(3)-C(2)	110.59(12)	C(8)-C(5)-C(6)	113.56(11)
C(4)-C(3)-B(1)	124.15(13)	O(2)-C(6)-C(9)	106.93(11)
C(2)-C(3)-B(1)	125.22(13)	O(2)-C(6)-C(10)	108.07(11)
C(3)-C(4)-C(1A)	113.39(11)	C(9)-C(6)-C(10)	110.67(12)
O(1)-C(5)-C(7)	108.53(11)	O(2)-C(6)-C(5)	102.34(10)
O(1)-C(5)-C(8)	106.43(11)	C(9)-C(6)-C(5)	113.49(12)
C(7)-C(5)-C(8)	110.17(12)	C(10)-C(6)-C(5)	114.59(12)
O(1)-C(5)-C(6)	102.47(10)	C(13)-C(12)-C(11)	114.86(12)
C(14)-C(13)-C(12)	110.73(13)	C(17)-C(15)-C(16)	113.30(11)
C(14)-C(13)-B(2)	124.44(13)	O(4)-C(16)-C(20)	106.76(11)
C(12)-C(13)-B(2)	124.81(13)	O(4)-C(16)-C(19)	108.29(11)
C(13)-C(14)-C(11A)	114.14(12)	C(20)-C(16)-C(19)	110.54(12)
O(3)-C(15)-C(18)	108.29(11)	O(4)-C(16)-C(15)	102.67(10)
O(3)-C(15)-C(17)	106.48(11)	C(20)-C(16)-C(15)	113.69(12)
C(18)-C(15)-C(17)	110.15(12)	C(19)-C(16)-C(15)	114.17(11)
O(3)-C(15)-C(16)	102.93(10)	O(2)-B(1)-O(1)	113.88(12)
C(18)-C(15)-C(16)	114.96(11)	O(2)-B(1)-C(3)	122.78(13)

Table 4-4. Bond lengths [Å] and angles [°] for complex **1**.

O(1)-B(1)-C(3)	123.32(13)
O(4)-B(2)-O(3)	113.87(13)
O(4)-B(2)-C(13)	123.36(13)
O(3)-B(2)-C(13)	122.74(13)
B(1)-O(1)-C(5)	106.84(10)
B(1)-O(2)-C(6)	107.20(11)
B(2)-O(3)-C(15)	107.33(11)
B(2)-O(4)-C(16)	107.30(11)

Table 4-5. Anisotropic displacement parameters ($\text{\AA}^2 \times 10^3$) for complex **1**. The anisotropic displacement factor exponent takes the form: $-2\pi^2 [h^2 a^{*2} U_{11} + \dots + 2 h k a^* b^* U_{12}]$.

	U ₁₁	U ₂₂	U ₃₃	U ₂₃	U ₁₃	U ₁₂
C(1)	33(1)	27(1)	41(1)	0(1)	-1(1)	-2(1)
C(1A)	24(1)	26(1)	20(1)	0(1)	4(1)	4(1)
C(2)	28(1)	22(1)	22(1)	1(1)	-2(1)	-2(1)
C(3)	15(1)	21(1)	20(1)	0(1)	-1(1)	-2(1)
C(4)	20(1)	25(1)	20(1)	1(1)	-1(1)	2(1)
C(5)	23(1)	21(1)	15(1)	-1(1)	1(1)	0(1)
C(6)	30(1)	20(1)	17(1)	-2(1)	3(1)	0(1)
C(7)	25(1)	22(1)	25(1)	-3(1)	1(1)	2(1)
C(8)	24(1)	28(1)	26(1)	-3(1)	-3(1)	-1(1)
C(9)	33(1)	27(1)	27(1)	-2(1)	8(1)	-7(1)
C(10)	46(1)	26(1)	19(1)	1(1)	0(1)	4(1)
C(11)	30(1)	33(1)	31(1)	2(1)	-4(1)	2(1)
C(11A)	22(1)	30(1)	29(1)	2(1)	2(1)	1(1)
C(12)	23(1)	27(1)	23(1)	0(1)	-2(1)	0(1)
C(13)	17(1)	27(1)	18(1)	-1(1)	-1(1)	1(1)
C(14)	22(1)	26(1)	22(1)	0(1)	0(1)	2(1)
C(15)	13(1)	23(1)	20(1)	-1(1)	-2(1)	0(1)
C(16)	16(1)	22(1)	25(1)	0(1)	0(1)	0(1)
C(17)	23(1)	29(1)	22(1)	2(1)	-1(1)	2(1)
C(18)	21(1)	32(1)	24(1)	-4(1)	1(1)	6(1)
C(19)	23(1)	29(1)	40(1)	-5(1)	-4(1)	-5(1)
C(20)	28(1)	33(1)	34(1)	10(1)	2(1)	-2(1)
B(1)	16(1)	21(1)	20(1)	0(1)	0(1)	0(1)
B(2)	19(1)	24(1)	16(1)	0(1)	0(1)	0(1)
O(1)	25(1)	20(1)	16(1)	0(1)	0(1)	1(1)
O(2)	32(1)	19(1)	17(1)	-2(1)	2(1)	2(1)
O(3)	15(1)	23(1)	25(1)	-3(1)	-1(1)	0(1)
O(4)	16(1)	21(1)	33(1)	-3(1)	1(1)	2(1)

Table 4-5. (cont.)

	U11	U22	U33	U23	U13	U12
S(1)	24(1)	26(1)	20(1)	0(1)	4(1)	4(1)
S(1A)	33(1)	27(1)	41(1)	0(1)	-1(1)	-2(1)
S(2)	22(1)	30(1)	29(1)	2(1)	2(1)	1(1)
S(2A)	30(1)	33(1)	31(1)	2(1)	-4(1)	2(1)

Table 4-6. Hydrogen coordinates ($\times 10^4$) and isotropic displacement parameters ($\text{\AA}^2 \times 10^3$) for complex **1**.

	x	y	z	U(eq)
H(1)	2340	2348	2701	40
H(1A)	1990	4599	2317	28
H(2)	2788	1236	1902	29
H(4)	2341	4224	1266	26
H(7A)	4262	160	249	36
H(7B)	3693	-32	-275	36
H(7C)	3399	-707	225	36
H(8A)	1737	-122	304	39
H(8B)	1858	386	-256	39
H(8C)	1451	1127	200	39
H(9A)	4390	3028	-66	43
H(9B)	4496	1838	-316	43
H(9C)	4598	1988	289	43
H(10A)	1957	2435	-367	45
H(10B)	2777	1881	-711	45
H(10C)	2872	3137	-544	45
H(11)	-340	-1066	3590	37
H(11A)	-312	1353	3697	32
H(12)	1520	-1539	3417	29
H(14)	1641	1766	3587	28
H(17A)	4492	-609	4176	37
H(17B)	5521	-962	3955	37
H(17C)	4644	-1812	3948	37
H(18A)	5005	-2035	3031	38
H(18B)	5758	-1047	2989	38
H(18C)	4814	-1054	2639	38
H(19A)	5252	1997	3642	46
H(19B)	5918	928	3632	46
H(19C)	5085	1043	4051	46

Table 4-6. (cont.)

	x	y	z	U(eq)
H(20A)	4257	680	2565	47
H(20B)	5373	887	2686	47
H(20C)	4604	1843	2778	47

Table 4-7. Crystal data and structure refinement for complex **2**.

X-ray ID	kub06	
Sample/notebook ID	TBADiol2	
Empirical formula	C ₆ H ₇ B O ₂ S	
Formula weight	153.99	
Temperature	208(2) K	
Wavelength	0.71073 Å	
Crystal system	Orthorhombic	
Space group	Pbca	
Unit cell dimensions	a = 6.460(12) Å	α = 90°
	b = 11.898(16) Å	β = 90°
	c = 20.82(3) Å	γ = 90°
Volume	1600(4) Å ³	
Z	8	
Density (calculated)	1.278 Mg/m ³	
Absorption coefficient	0.338 mm ⁻¹	
F(000)	640	
Crystal size	0.50 x 0.20 x 0.02 mm ³	
Crystal color/habit	colorless plate	
Theta range for data collection	3.42 to 27.44°	
Index ranges	-3 ≤ h ≤ 8, -14 ≤ k ≤ 12, -26 ≤ l ≤ 26	
Reflections collected	7789	
Independent reflections	1763 [R(int) = 0.0323]	
Completeness to theta = 25.00°	99.9 %	
Absorption correction	Semi-empirical from equivalents	
Max. and min. transmission	0.9933 and 0.8490	
Refinement method	Full-matrix least-squares on F ²	
Data / restraints / parameters	1763 / 0 / 92	
Goodness-of-fit on F ²	1.084	
Final R indices [I > 2σ(I)]	R1 = 0.0575, wR2 = 0.1566	
R indices (all data)	R1 = 0.0654, wR2 = 0.1663	
Largest diff. peak and hole	0.499 and -0.354 e.Å ⁻³	

Table 4-8. Atomic coordinates ($\times 10^4$) and equivalent isotropic displacement parameters ($\text{\AA}^2 \times 10^3$) for complex **2**. $U(\text{eq})$ is defined as one third of the trace of the orthogonalized U_{ij} tensor.

	x	y	z	U(eq)
C(1)	1099(2)	8187(1)	3298(1)	67(1)
C(1A)	1291(1)	8501(1)	4101(1)	60(1)
C(2)	2932(3)	7297(2)	3170(1)	55(1)
C(3)	4100(3)	7026(1)	3740(1)	44(1)
C(4)	3323(3)	7633(1)	4284(1)	49(1)
C(5)	8670(3)	5002(2)	3414(1)	59(1)
C(6)	8889(3)	5216(2)	4152(1)	65(1)
B(1)	6052(3)	6210(2)	3759(1)	44(1)
O(1)	6800(2)	5638(1)	3220(1)	59(1)
O(2)	7189(2)	6008(1)	4317(1)	66(1)
S(1)	1291(1)	8501(1)	4101(1)	60(1)
S(1A)	1099(2)	8187(1)	3298(1)	67(1)

Table 4-9. Bond lengths [Å] and angles [°] for complex **2**.

C(1)-C(2)	1.611(3)	C(5)-O(1)	1.482(3)
C(1A)-C(4)	1.713(3)	C(5)-C(6)	1.565(3)
C(2)-C(3)	1.442(3)	C(6)-O(2)	1.487(3)
C(3)-C(4)	1.435(3)	B(1)-O(2)	1.396(3)
C(3)-B(1)	1.592(3)	B(1)-O(1)	1.398(3)
C(3)-C(2)-C(1)	113.38(15)		
C(4)-C(3)-C(2)	110.69(18)		
C(4)-C(3)-B(1)	124.40(16)		
C(2)-C(3)-B(1)	124.85(16)		
C(3)-C(4)-C(1A)	113.32(15)		
O(1)-C(5)-C(6)	104.97(15)		
O(2)-C(6)-C(5)	105.23(15)		
O(2)-B(1)-O(1)	113.72(18)		
O(2)-B(1)-C(3)	122.85(16)		
O(1)-B(1)-C(3)	123.42(16)		
B(1)-O(1)-C(5)	108.16(16)		
B(1)-O(2)-C(6)	107.82(16)		

Table 4-10. Anisotropic displacement parameters ($\text{\AA}^2 \times 10^3$) for complex **2**. The anisotropic displacement factor exponent takes the form: $-2\pi^2 [h^2 a^{*2} U_{11} + \dots + 2 h k a^* b^* U_{12}]$

	U ₁₁	U ₂₂	U ₃₃	U ₂₃	U ₁₃	U ₁₂
C(1)	69(1)	70(1)	63(1)	1(1)	-10(1)	9(1)
C(1A)	62(1)	60(1)	58(1)	-3(1)	5(1)	5(1)
C(2)	57(1)	64(1)	45(1)	-5(1)	1(1)	-1(1)
C(3)	45(1)	42(1)	46(1)	0(1)	3(1)	-5(1)
C(4)	52(1)	49(1)	45(1)	-1(1)	2(1)	1(1)
C(5)	49(1)	60(1)	67(1)	-3(1)	3(1)	7(1)
C(6)	55(1)	71(1)	70(1)	-4(1)	-8(1)	12(1)
B(1)	46(1)	41(1)	45(1)	-1(1)	2(1)	-7(1)
O(1)	57(1)	68(1)	51(1)	-7(1)	1(1)	14(1)
O(2)	65(1)	80(1)	53(1)	-9(1)	-8(1)	19(1)
S(1)	62(1)	60(1)	58(1)	-3(1)	5(1)	5(1)
S(1A)	69(1)	70(1)	63(1)	1(1)	-10(1)	9(1)

Table 4-11. Hydrogen coordinates ($\times 10^4$) and isotropic displacement parameters ($\text{\AA}^2 \times 10^3$) for complex **2**.

	x	y	z	U(eq)
H(1)	140	8471	2999	81
H(1A)	519	8995	4360	72
H(2)	3212	6985	2765	66
H(4)	3875	7562	4700	58
H(5A)	9893	5275	3183	71
H(5B)	8497	4198	3325	71
H(6A)	8743	4512	4392	78
H(6B)	10240	5548	4252	78

4.4 Conductometric Measurements

The discovery of conducting polymers has led to a surge in the amount of research in the field due to the amount of potential organic conductors can have on the electronics industry. Further discoveries in modified organic conductors has led to their development in light emitting diodes (LEDs), sensors, and other microelectronic devices. Their use as sensor elements is the focus of this research.

Movement of charge within polymers occurs via a bipolaron pathway. A bipolaron is a result of two polarons coming close together and interacting such that the resulting bipolaron state is more stable than the two polarons on their own. A polaron is a result of a lattice distortion due to the introduction of charge within a matrix. The lattice distortion is a compensation within the matrix to shield the charge from the rest of the matrix. The lattice distortion also acts as a potential well that hinders movement of the charge within the matrix. In conducting polymer matrices, the stability of bipolaron states as well as the distances between the states due to electron hopping, control the matrices ability to conduct electrons. As a result of this, control over the distances between bipolaron states and a molecule's ability to stabilize a bipolaron state can lead to control over the polymer matrix's ability to conduct electrons.

Polythiophenes are well studied conducting polymers that have been used for interconnects, LEDs, and sensors. As sensors, polythiophenes and their derivatives have been used for detection of NO_x and volatile organic compounds. The main mechanism for a change in conduction has been attributed to a

swelling of the polymer resulting in an increase in the distance between polymer chains. The increase means that there is a larger distance for the electron to hop between chains thus resulting in an increase in resistance within the polymer matrix.

Polymerization of conducting polymers such as thiophenes can be done be either chemical¹³⁻¹⁶ or electrochemical^{17, 18} means. Chemical polymerization of thiophenes occurs with FeCl_3 ^{19, 20} but results in uncontrolled polymerization leading to the formation of both head-to-tail and head-to-head polymers. Others have shown that is possible to control the formation of primarily head-to-tails polymers via a Grignard mechanism²¹. In the electrochemical polymerization of thiophenes, polymerization can be done either anodically¹⁷ or cathodically¹⁸. Anodic polymerization results in poorly conducting, unstable polymers. Cathodic polymerization of thiophene results in the formation of the conducting polythiophene via a radical initiation though this method also suffers from uncontrolled polymerization resulting in the formation of both head-to-tail and head-to-head polymers. We have polymerized thiophenes via a cathodic electrochemical polymerization method primarily because we can directly polymerize the thiophene onto the interdigitated electrode, creating an ideal sensing platform in a single step.

We postulated that the interaction of the poly thiophene 3-boronic acid with a diol such as glucose will result in an observable change in the conduction of current through the polymer matrix. Polymerized thiophene 3-boronic acid was used as the sensing element due to the ease of polymerization of the

polythiophene and the boronic acid group's high affinity for diols such as glucose. Boronic acid binding to diols via ester linkages has been known for quite a while now^{9, 22-27}, but has only been exploited in recent years²⁸⁻³⁶.

4.5 Experimental

Alizarin Red S. was purchased from Acros and used as received with no further purification necessary. Thiophene 3-boronic acid, and glucose were purchased from Aldrich used as received with no further purification. All solvents were purchased from Aldrich and were HPLC grade.

4.5.1 Electrochemical Polymerization of Thiophene 3-Boronic Acid

Polymerization of thiophene 3-boronic acid onto a platinum-wire was done by cyclic voltammetry *via* a 3-electrode system using a BAS Electronics Potentiostat. Platinum wires were used for working and counter electrodes. 0.1 M solution of thiophene 3-boronic acid was made in 0.1 M tetrabutyl ammonium hexafluorophosphate in acetonitrile from a custom solvent system. The 0.1M TBA solution was cycled 4 times from 1000mV to 2500mV at a rate of 50mV/second resulting in the formation of black layers of polythiophene 3-boronic acid onto the electrode surface. The initiation step of the radical chain polymerization occurs at 1600mV (vs. Fc/Fc⁺ reference electrode).

4.5.2 Elemental analysis of poly-Thiophene Boronic Acid

Elemental analysis of poly-Thiophene Boronic Acid was done by Midwest Microscience

4.5.3 Fluorescence Studies of poly-Thiophene 3-Boronic Acid with Alizarin Red S

Poly-thiophene 3-boronic acid coated electrodes was soaked in 1.0mM Alizarin Red S solution in DPBS at pH 7.4. Electrode was rinsed with DPBS solution followed by 17.9M Ω water and dried and dried with N₂. Polymer was mechanically removed and placed on borosilicate slide. a polymer was irradiated with 530nm light and fluorescence was observed at 570nm using a fluorescence microscope

4.5.4 Electrochemical Polymerization of Thiophene 3-Boronic Acid onto Interdigitated Electrode

Polymerization of thiophene 3-boronic acid onto the interdigitated electrode was done by cyclic voltammetry *via* a 3-electrode system using a BAS Electronics Potentiostat.

Initially only one side of the interdigitated electrode was connected as the working electrode. The counter and reference electrode were Pt wire and Fc/Fc⁺, respectively.

0.1 M solution of thiophene 3-boronic acid was made in 0.1 M tetrabutyl ammonium hexafluorophosphate in acetonitrile from a custom solvent system.

The system was cycled 1000mV to 2500mV at a rate of 50mV/second resulting in the formation of black layers of polythiophene 3-boronic acid onto the electrode surface. The initiation step of the radical chain polymerization occurs at 1600mV (vs. Fc/Fc⁺ reference electrode). The interdigitated electrodes were mounted to a custom made cell **Figure 4-12**. The cell is composed of a Teflon

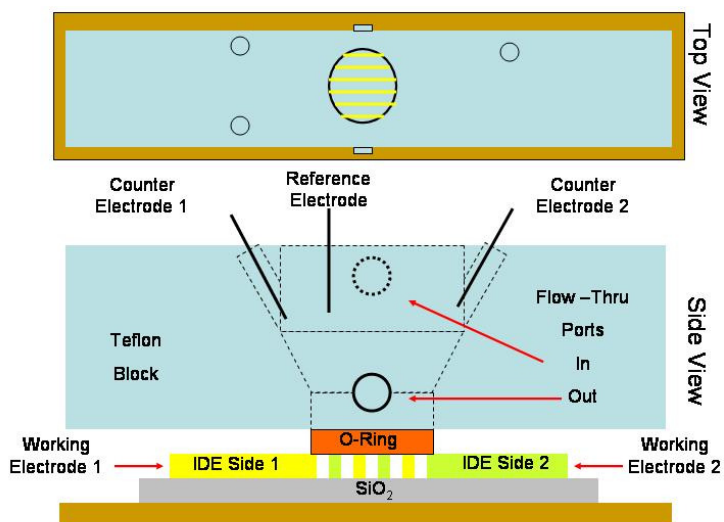


Figure 4-12 – Schematic of custom made flow cell used for both electrochemical polymerization of TBA onto the interdigitated electrode platform and modified for use in the detection of diols.

block with a hole drilled completely through it to serve as a well to hold the solution of the monomer over the interdigitated fingers. The well is formed by sandwiching an o-ring between the Teflon block and the fingers of the interdigitated electrodes. Five additional holes were drilled into the well, two of the holes serve as entrance and exit holes for flowing solution through the cell, and the other three act as a holder for the two counter electrodes and the reference electrode. The interdigitated electrodes were connected via wires that

were silver painted onto each set of interdigitated electrodes. Epoxy was used for added strength to the wire-electrode interconnect.

Polymerization of thiophene 3-boronic acid across the interdigitated electrodes was done with two Pine Instruments Bipotentiostats *via* a two working electrode system

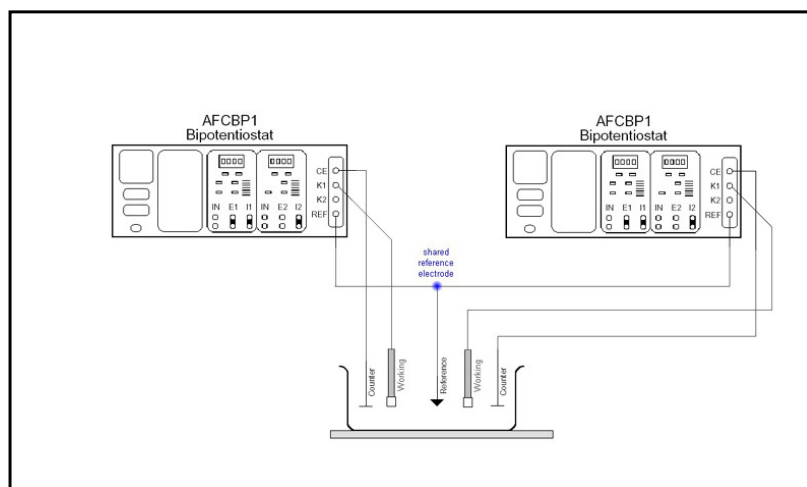


Figure 4-13 – Dual Pine Instruments Potentiostat set up for dendritic growth of TBA across interdigitated electrodes. System employs a shared reference electrode.

Figure 4-13 where each system is held at opposing potentials to the other.

4.5.5 Atomic Force Microscopy

Atomic force microscopy measurements was done using a Digital Instruments Nanoscope III with an Extended MultiMode Head in tapping mode.

4.6 Results and Discussion

The polymer film was characterized by elemental analysis **Table 4-12** and exhibited carbon and hydrogen ratios that were within expected values for a polythiophene based polymer. Mass spectrometry of polythiophene 3-boronic acid was unattainable due to insolubility in all solvents tried.

Table 4-12 - Elemental analysis of polythiophene boronic acid

	Number of Subunits	% Carbon	% Hydrogen	%C:%H
Theoretical	1	54.63	6.42	8.51
	2	37.84	3.18	11.9
	3	37.94	2.92	12.99
	4	37.99	2.79	13.62
	5	38.02	2.71	14.03
	6	38.05	2.66	14.3
Measured		36.98		13.16
		36.48		14.19

4.6.1 Exposure of Thiophene 3-Boronic Acid polymer to Alizarin Red S for Fluorescence Studies

As shown previously, exposure of TBA to ARS results in a fluorescence emission due to formation of an ARS-TBA complex Figure 4-3. As expected the ARS exposed p-TBA coated electrode emitted a fluorescence peak at 570nm giving definitive proof that the ARS readily binds to the boronic acid groups of polythiophene 3-boronic acid. Images of the polymers were used to compare the fluorescence of polythiophene 3-boronic acid and ARS exposed polythiophene 3-boronic acid **Figure 4-14**.



Figure 4-14 – Image of polythiophene-3-boronic acid (top) and fluorescence image after exposure to Alizarin Red S (bottom).

The control, a polythiophene 3-boronic acid coated electrode that was not exposed to the Alizarin Red S, did not display fluorescence.

4.6.2 Interdigitated Electrode Sensing Platform

Interdigitated electrodes composed of 150nm thick gold fingers that are 10 μ m wide with 10 μ m gaps between the fingers **Figure 4-15** were fabricated as stated in Chapter 2-Fabrication of Interdigitated Electrodes. Exhibition of polymerization onto the electrode

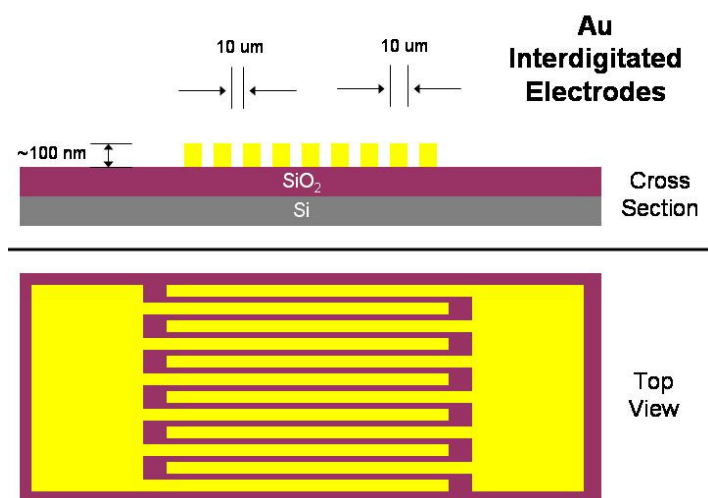


Figure 4-15 – Schematic of Au interdigitated Electrodes 10μm separation between electrode fingers

surface was done by polymerizing the thiophene 3-boronic acid onto a single electrode of the interdigitated array. Atomic force microscopy was used to show the differences in the individual fingers of the electrodes polymer coated versus non polymer coated and show a 50 nm increased thickness in the polymer coated electrode versus bare electrode **Figure 4-16**.

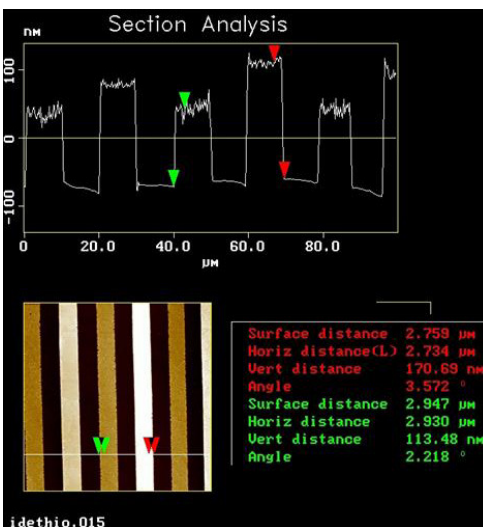


Figure 4-16 – Atomic force images of polythiophene 3-boronic acid coated and uncoated electrodes

4.6.3 Electrochemical Polymerization of Thiophene 3-Boronic Acid onto Interdigitated Electrodes

Polymerization across the electrodes was achieved using a dendritic growth method employed by Sailor et al³⁷. Each system is composed of a set of interdigitated fingers as the working electrode, a platinum counter electrode, and a shared Ag wire pseudo electrode. The system is cycled from 1000mV to 2500mV potentials at a rate of 100mV/second **Figure 4-16**. The radical polymerization initiates at 1800mV

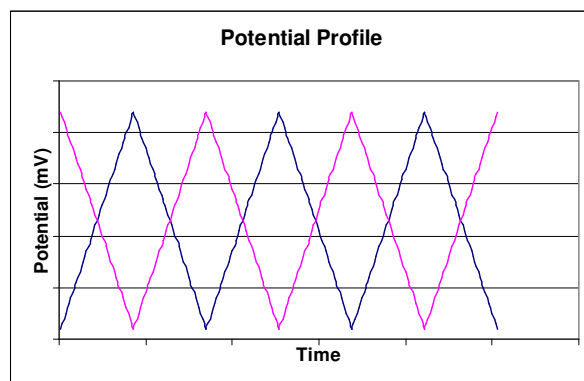


Figure 4-17 – Potential Profile applied to opposing electrodes to induce dendritic growth of p-TBA

(vs Ag/AgCl reference electrode). Current response must be monitored for the jump in current which corresponds to the time at which electrical connection is completed between the two opposing electrodes.

The rapid dendritic growth observed for the polymerization of the polythiophene-3-boronic acid results in black polymer that spans the gap between electrodes. The black polymer exhibits resistances from 3Ω to $20\text{ k}\Omega$. Attempts to control polymer growth for the purpose of forming more consistent films, done by changing the total polymerization time and solution concentrations, were unsuccessful based on the instrumentation used.

4.6.4 Conditioning of the p-TBA on the Interdigitated Electrodes

After polymerization, the cell is modified by plugging the top of the well and the holes used for holding the counter and reference electrodes **Figure 4-17**.

This is done so that

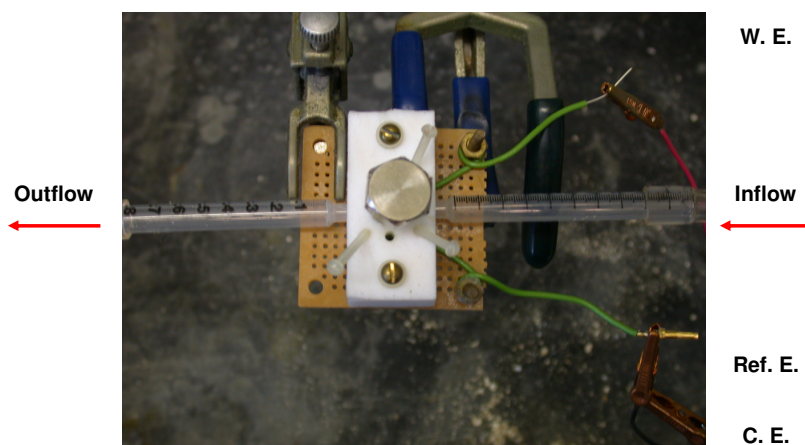


Figure 4-18 – Modified flow cell for glucose detection

the cell can serve as a flow cell where solution can be flowed over the system while monitoring the current change under a constant applied potential. The polymer is conditioned by running a constant flow of DPBS (pH 7.4) through the cell while monitoring a change in current under a 150mV applied potential. Conditioning, which establishes a baseline current takes approximately 30 minutes.

4.6.5 Electrochemical Detection of Diols

The electrochemical detection of diols on the p-TBA was done by monitoring the change in current under an applied bias of 150mV across the

electrodes. This was achieved by setting up Bioanalytic Systems Potentiostat to measure current *via* a two electrode set-up. A pH 7.4 buffer is flowed across until a baseline current is established. After a baseline is established the systems response to successive 5mL injections of the DPBS were measured

Figure 4-18. The system shows an initial increase in current as the

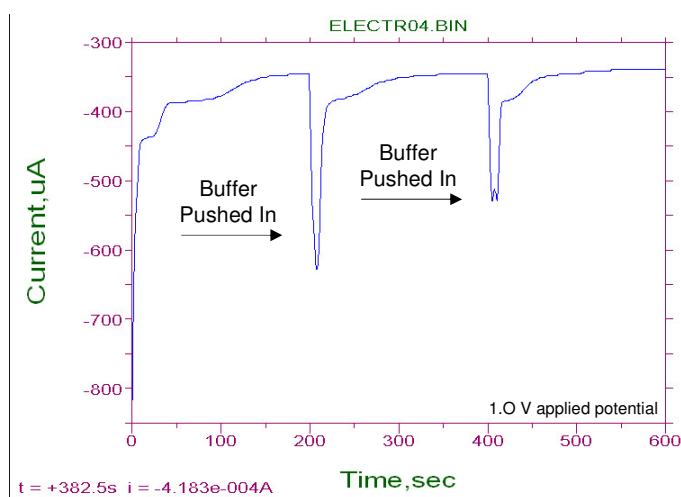


Figure 4-19 – Current response to 5ml injections of DPBS (pH 7.4) at 150mV applied potential

DPBS solution was pushed into the flow cell. The initial increase in current is due to the increase in flow of solution through the cell. The system then slowly returns back to baseline current conditions. Several injections of the DPBS show that the systems response is consistent. The cell was then injected with a series of 5mL solutions: 1mM glucose in DPBS (pH 7.4), DPBS, 1mM glucose in DPBS (pH 7.4), and DPBS, while monitoring the current. In the case of glucose solution injection the same initial increase in current was exhibited as seen in the injection of DPBS into the system that correlates to the increased flow of solution into the system. Interestingly though, the system never

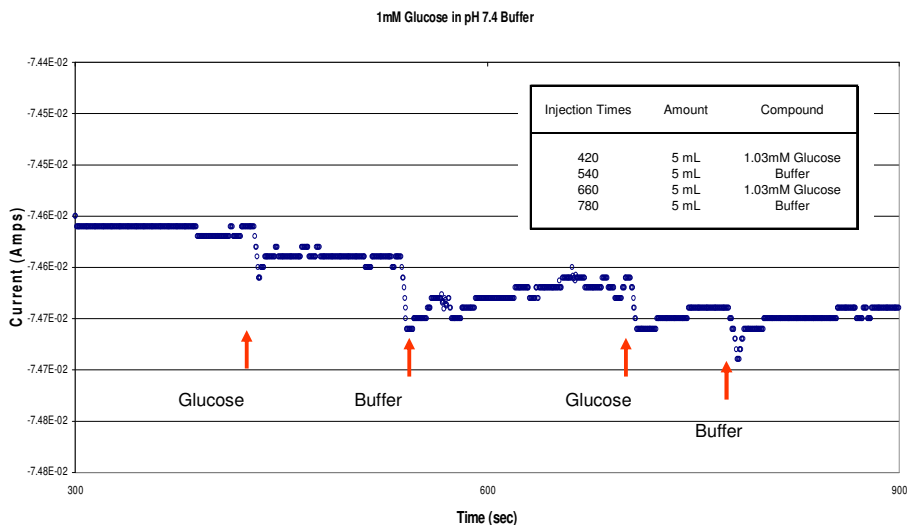


Figure 4-20 – Current response to injections of .03mM glucose of DPBS (pH 7.4) at 150mV applied potential

returns back to baseline even after long wait times after injection (>30 minutes). A return to baseline would indicate a complete disassociation of the glucose from the polymer, after the initial associative process. A change in current from baseline to after injection was observed ($30\mu\text{A}$) and can be attributed to the binding of glucose to the p-thiophene-3-boronic acid **Figure 4-19**. The subsequent injection of DPBS exhibited the same initial increase in current followed by a slow return to baseline. The process was repeated resulting in a consistent response by the cell. Similar series of injections were done using 5mM and 10mM glucose in DPBS (pH 7.4). The cells exhibited similar response but with a larger magnitude ($100\mu\text{A}$ and $150\mu\text{A}$, respectively). In these cases, the system appears to immediately saturate since subsequent injections of DPBS and glucose results in no cell response.

There are two different observations in the current response of glucose exposure to the polythiophene 3-boronic acid. Initially buffer is static over the conducting polymer, thus electron transport from the one electrode to the polymer and over to the opposing electrode is diffusion limited. During injection of buffer into the sample cell, the rate of electron transport is no longer diffusion limited. Thus the initial increase in current is a result of ion flux from the injection of NPBS.

The more significant observation is that with the introduction of glucose into the sample cell, a change in the baseline current is also observed. Supported by observations from previous experiments: 1) diols readily bind to the polythiophene 3-boronic acid (Fluorescence Studies of Diols to Poly Thiophene 3-Boronic Acid and X-Ray Crystal Structures of Thiophene 3-Boronic Acid with various Diols), and 2) diols such as glucose have a high affinity to thiophene 3-boronic acid (Fluorescence Binding Studies of Thiophene 3-Boronic Acid to Various Diols), the observed increase in current can be attributed to boronic ester formation, resulting in a conformation change within the polymer. The conformational change can either increase or decrease in current depending on the mechanism of electron transport.

If the mode of transport is due to mass transport, then we can infer that the observed increase in current is due to shrinking of the polymer that can be attributed to decrease in the amount of solvent within the polymer matrix. This can readily be confirmed by measuring changes in polymer thickness before and after exposure.

Alternatively, the formation of the boronic ester may also shift the conducting polymers electronic structure enough resulting in an increase in current.

4.7 Conclusion

We have definitively shown, chemically, optically and electronically, that exposure of the polythiophene 3-boronic acid to a diol will result in binding of the diol to the boronic acid moiety. Optically, the polythiophene 3-boronic acid exhibited the expected fluorescence upon exposure to the Alizarin Red S dye. Electronically, the polythiophene 3-boronic acid exhibits a change in current upon exposure to glucose in the DPBS. The polymer also exhibits a linear response to increasing concentrations of glucose.

We believe that it is also likely that the ester linkage formed by the boronic acid and the diol stabilizes the conducting modes of the polythiophene backbone resulting in an increase in conduction but requires further investigation. Clearly this demonstrates that polythiophene 3-boronic acid can be used as a medium for glucose sensing.

REFERENCES

1. Singaram, B. C., Jason N.; Suri, Jeff T.; Cappuccio, Frank E.; Wessling, Ritchie A.; Singaram, Bakthan., Boronic acid substituted viologen based optical sugar sensors: modulated quenching with viologen as a method for monosaccharide detection. *Tetrahedron Letters* **2002**, 43, (7), 1139-1141.
2. Singaram, B. C., D. B.; Gamsey, S.; Sharrett, Z.; Miller, A.; Thoniyot, P.; Wessling, R. A., The Interaction of Boronic Acid-Substituted Viologens with Pyranine: The Effects of Quencher Charge on Fluorescence Quenching and Glucose Response. *Langmuir* **2005**, 21, 6540-6547.
3. Singaram, B. C., David B.; Miller, Aaron; Gamsey, Soya; Sharrett, Zach; Thoniyot, Praveen; Wessling, Ritchie; , Optical glucose detection across the visible spectrum using anionic fluorescent dyes and a viologen quencher in a two-component saccharide sensing system. *Organic & Biomolecular Chemistry* **2005**, 3, (9), 1708-1713.
4. Borba, E. B. d.; Amaral, C. L. C.; Politi, M. J.; Vallalobos, R.; Baptista, M. S., Photophysical and Photochemical Properties of Pyranine/Methyl Viologen Complexes in Solution and in Supramolecular Aggregates: A Switchable Complex *Langmuir* **2000**, 16, 5900 - 5907.
5. Shoji, E. a. F., Michael S., Poly(aniline boronic acid): A New Precursor to Substituted Poly(aniline)s. *Langmuir* **2001**, 17, (23), 7183-7185.
6. Shoji, E. a. F., Michael S. , Potentiometric Saccharide Detection Based on the pKa Changes of Poly(aniline boronic acid). *Journal of the American Chemical Society* **2002**, 124, 12486-12493.
7. Springsteen, G. a. W., B., A Detailed Examination of Boronic Acid-Diol Complexation. *Tetrahedron* **2002**, 58, 5291-5300.
8. Kayakina, E. E. A. A. K., Olga V. Gitelmacher,, Prussian Blue-Based First-Generation Biosensor. A Sensitive Amperometric Electrode for Glucose. *Analytical Chemistry* **1995**, 67, 2419-2423.
9. Wang, B. K., V.; Gao, X.; Gao, S.; Yang, W.; Sabapathy, S.; Ni, W., A Glucose-Selective Fluorescence Sensor Based on Boronic Acid-Diol Recognition. *Bioorganic & Medicinal Chemistry Letters* **2002**, 12, (23), 3373-3377.
10. Wang, B. F., H.; Kaur, G., Progress in Boronic Acid-Based Fluorescent Glucose Sensors. *Journal of Fluorescence* **2004**, 14, (5), 481-489.

11. Wang, B. Y., W.; Lin, L., A Novel Type of Fluorescent Boronic Acid for Carbohydrate Recognition. *Tetrahedron Letters* **2005**, 46, 7981-7984.
12. Benesi, H.; Hildebrand, J., A Spectrophotometric Investigation of the Interaction of Iodine with Aromatic Hydrocarbons. *Journal of the American Chemical Society* **1949**, 71, (8), 2703-2707.
13. Kagan, f. A., S. K. 1983,20, 1937, *Heterocycles* **1983**, 20, 1937.
14. Kagan, J.; Arora, S. K., The synthesis of alpha-thiophene oligomers via organoboranes. *Tetrahedron Letters* **1983**, 24, 4043.
15. Steinkopft, W.; Leitsmann, R.; Hofmann, K. H., Studien in der Thiophenreihe. LVII '1. Uber a-Pobthiensele. *Liebigs Ann. Chem.* **1941**, 546, 180.
16. Wynber, H.; Metaelaar, J., A Convenient Route To Polythiophenes *Synthetic Communications* **1984**, 14, 1-9.
17. Tourillon, G.; Garnier, F., *J. Electroanal. Chem.* **1982**, 135, 173.
18. Zotti, G.; Schiavon, G., *J. Electroanal. Chem* **1984**, 163, 385.
19. Bizzarri, P. C.; Andreani, F.; Della Casa, C.; Lanzi, M.; Salatelli, E., Ester-functionalized poly(3-alkylthienylene)s: substituent effects on the polymerization with FeCl₃. *Synthetic Metals* **1995**, 75, (2), 141-147.
20. Fraleoni-Morgera, A.; Della Casa, C.; Lanzi, M.; Bizzarri, P. C., Investigation on Different Procedures in the Oxidative Copolymerization of a Dye-Functionalized Thiophene with 3-Hexylthiophene *Macromolecules* **2003**, 36, 8617-8620.
21. McCullough, R. D.; Lowe, R. D., *Chem. Commun.* **1992**, 70-72.
22. Bagshawe, K. D., Antibody-directed enzyme prodrug therapy: A review. *Drug Dev. Res.* **1995**, 34, (2), 220-230.
23. Butle, J. W. M.; Hoeckstra, Y.; Kamman, R. L.; Magin, R. L.; Webb, A. G.; Briggs, R. W.; Go, K. G.; Hulstaert, C. E.; Miltenyi, S.; The, T. H.; Leij., L. D., Specific MR imaging of human lymphocytes by monoclonal antibody-guided dextran-magnetite particles. *Magn. Reson. Med.* **1992**, 25, (1), 148-157.
24. Friden, P. M.; Walus, L. R.; Musso, G. F.; Taylor, M. A.; Malfroy, B.; Starzyk., R. M., Anti-Transferrin Receptor Antibody and Antibody-Drug Conjugates Cross the Blood-Brain Barrier *Proc. Natl Acad. Sci.* **1991**, 88, (11), 4771-4775.

25. Kuan, C. T.; Pastan, I., Improved antitumor activity of a recombinant anti-Lewis^y immunotoxin not requiring proteolytic activation *Proceedings of the National Academy of Sciences* **1996**, 93, (3), 974-978.
26. Springer, C. J.; Niculescu-Duvaz, I.; Pedley, R. B., Novel Prodrugs of Alkylating Agents Derived from 2-Fluoro- and 3-Fluorobenzoic Acids for Antibody-Directed Enzyme Prodrug Therapy. *J. Med. Chem.* **1994**, 37, (15), 2361-2370.
27. Tiefenauer, L. X.; Kuhne, G.; Andrea, R. Y., Antibody-magnetite nanoparticles: In vitro characterization of a potential tumor-specific contrast agent for magnetic resonance imaging. *Bioconjugate Chemistry* **1993**, 4, 347-352.
28. Adhikiri, D. P.; Heagy, M. D., Fluorescent chemosensor for carbohydrates which shows large change in chelation-enhanced quenching. *Tetrahedron Letters* **1999**, 40, (45), 7893-7896.
29. Arimori, S.; Bosch, L. I.; Ward, C. J.; James, T. D., Fluorescent internal charge transfer (ICT) saccharide sensor. *Tetrahedron Lett.* **2001**, 42, (27), 4553-4555.
30. Cabell, L. A.; Monahan, M.-K.; Anslyn, E. V., A competition assay for determining glucose-6-phosphate concentration with a tris-boronic acid receptor. *Tetrahedron Letters* **1999**, 40, (44), 7753-7756.
31. Eggert, H.; Frederiksen, J.; Morin, C.; Norrild, J. C., A New Glucose-Selective Fluorescent Bisboronic Acid. First Report of Strong α -Furanose Complexation in Aqueous Solution at Physiological pH1 *Journal of Organic Chemistry* **1999**, 64, (11), 3846-3852.
32. James, D.; Sandanayake, K. R. A. S.; Iguchi, R.; Shinkai, S., Novel Saccharide-Photoinduced Electron Transfer Sensors Based on the Interaction of Boronic Acid and Amine *J. Am. Chem. Soc.* **1995**, 117, (35), 8982-8987.
33. James, T. D.; Sandanayake, K. R. A. S.; Shinkai, S., Saccharide Sensing with Molecular Receptors Based on Boronic Acid. *Angewandte Chemie International Edition* **1996**, 35, (17), 1910-1922.
34. Wang, W.; Gao, S.; Wang, B., Building Fluorescent Sensors by Template Polymerization: The Preparation of a Fluorescent Sensor for D-Fructose *Org. Lett.* **1999**, 1, (8), 1209-1212.
35. Yang, W.; He, H.; Drueckhammer, D. G., Computer-Guided Design in Molecular Recognition: Design and Synthesis of a Glucopyranose Receptor. *Angewandte Chemie International Edition* **2001**, 40, (9), 1714-1718.

36. Czarnik, A. W. a. Y., Juyoung; and Fluorescent Chemosensors of Carbohydrates. A Means of Chemically Communicating the Binding of Polyols in Water Based on Chelation-Enhanced Quenching. *Journal of the American Chemical Society* **1992**, 114, 5874-5875.
37. Sailor, M. J.; Curtis, C. L., Conducting Polymer Connections for Molecular Devices. *Advanced Materials* **1994**, 6, (9), 688-692.